



# ODIN: Improved Narrowband Ly $\alpha$ Emitter Selection Techniques for $z = 2.4, 3.1$ , and $4.5$

Nicole M. Firestone<sup>1</sup> , Eric Gawiser<sup>1</sup> , Vandana Ramakrishnan<sup>2</sup> , Kyoung-Soo Lee<sup>2</sup> , Francisco Valdes<sup>3</sup> , Changbom Park<sup>4</sup> , Yujin Yang<sup>5</sup> , Robin Ciardullo<sup>6,7</sup> , María Celeste Artale<sup>8</sup> , Barbara Benda<sup>1,9</sup>, Adam Broussard<sup>1</sup>, Lana Eid<sup>1</sup>, Rameen Farooq<sup>1</sup>, Caryl Gronwall<sup>6,7</sup> , Lucia Guaita<sup>8</sup> , Stephen Gwyn<sup>10</sup> , Ho Seong Hwang<sup>11,12</sup> , Sang Hyeok Im<sup>11</sup> , Woong-Seob Jeong<sup>5</sup> , Shreya Karthikeyan<sup>13</sup> , Dustin Lang<sup>14</sup> , Byeongha Moon<sup>5</sup> , Nelson Padilla<sup>15</sup> , Marcin Sawicki<sup>16</sup> , Eunsuk Seo<sup>17</sup> , Akriti Singh<sup>18,19</sup>, Hyunmi Song<sup>17</sup> , and Paulina Troncoso Iribarren<sup>20</sup>

<sup>1</sup> Department of Physics and Astronomy, Rutgers, The State University of New Jersey, Piscataway, NJ 08854, USA

<sup>2</sup> Department of Physics and Astronomy, Purdue University, 525 Northwestern Ave., West Lafayette, IN 47906, USA

<sup>3</sup> NSF's National Optical-Infrared Astronomy Research Laboratory, 950 N. Cherry Ave., Tucson, AZ 85719, USA

<sup>4</sup> Korea Institute for Advanced Study, 85 Hoegi-ro, Dongdaemun-gu, Seoul 02455, Republic of Korea

<sup>5</sup> Korea Astronomy and Space Science Institute, 776 Daedeokdae-ro, Yuseong-gu, Daejeon 34055, Republic of Korea

<sup>6</sup> Department of Astronomy & Astrophysics, The Pennsylvania State University, University Park, PA 16802, USA

<sup>7</sup> Institute for Gravitation and the Cosmos, The Pennsylvania State University, University Park, PA 16802, USA

<sup>8</sup> Universidad Andres Bello, Facultad de Ciencias Exactas, Departamento de Física, Instituto de Astrofísica, Fernandez Concha 700, Las Condes, Santiago (RM), Chile

<sup>9</sup> Department of Physics, University of Washington, Seattle, WA 98195, USA

<sup>10</sup> Herzberg Astronomy and Astrophysics Research Centre, National Research Council of Canada, Victoria, British Columbia, Canada

<sup>11</sup> Department of Physics and Astronomy, Seoul National University, 1 Gwanak-ro, Gwanak-gu, Seoul 08826, Republic of Korea

<sup>12</sup> SNU Astronomy Research Center, Seoul National University, 1 Gwanak-ro, Gwanak-gu, Seoul 08826, Republic of Korea

<sup>13</sup> Department of Astronomy, University of Maryland, College Park, MD 20742, USA

<sup>14</sup> Perimeter Institute for Theoretical Physics, 31 Caroline St. North, Waterloo, ON N2L 2Y5, Canada

<sup>15</sup> Instituto de Astronomía Teórica y Experimental (IATE), CONICET-UNC, Laprida 854, X500BGR, Córdoba, Argentina

<sup>16</sup> Institute for Computational Astrophysics and Department of Astronomy and Physics, Saint Mary's University, 923 Robie St., Halifax, Nova Scotia, B3H 3C3, Canada

<sup>17</sup> Department of Astronomy and Space Science, Chungnam National University, 99 Daehak-ro, Yuseong-gu, Daejeon 34134, Republic of Korea

<sup>18</sup> Departamento de Ciencias Fisicas, Universidad Andres Bello, Fernandez Concha 700, Las Condes, Santiago, Chile

<sup>19</sup> European Southern Observatory Las Condes, Región Metropolitana, Chile

<sup>20</sup> Escuela de Ingeniería, Universidad Central de Chile, Avenida Francisco de Aguirre 0405, 171-0164 La Serena, Coquimbo, Chile

Received 2023 December 22; revised 2024 August 2; accepted 2024 August 19; published 2024 October 14

## Abstract

Lyman-alpha-emitting galaxies (LAEs) are typically young, low-mass, star-forming galaxies with little extinction from interstellar dust. Their low dust attenuation allows their Ly $\alpha$  emission to shine brightly in spectroscopic and photometric observations, providing an observational window into the high-redshift Universe. Narrowband surveys reveal large, uniform samples of LAEs at specific redshifts that probe large-scale structure and the temporal evolution of galaxy properties. The One-hundred-deg $^2$  DECam Imaging in Narrowbands (ODIN) utilizes three custom-made narrowband filters on the Dark Energy Camera (DECam) to discover LAEs at three equally spaced periods in cosmological history. In this paper, we introduce the hybrid-weighted double-broadband continuum estimation technique, which yields improved estimation of Ly $\alpha$  equivalent widths. Using this method, we discover 6032, 5691, and 4066 LAE candidates at  $z = 2.4, 3.1$ , and  $4.5$  in the extended COSMOS field ( $\sim 9$  deg $^2$ ). We find that [O II] emitters are a minimal contaminant in our LAE samples, but that interloping Green Pea-like [O III] emitters are important for our redshift 4.5 sample. We introduce an innovative method for identifying [O II] and [O III] emitters via a combination of narrowband excess and galaxy colors, enabling their study as separate classes of objects. We present scaled median stacked spectral energy distributions for each galaxy sample, revealing the overall success of our selection methods. We also calculate rest-frame Ly $\alpha$  equivalent widths for our LAE samples and find that the EW distributions are best fit by exponential functions with scale lengths of  $w_0 = 53 \pm 1$ ,  $65 \pm 1$ , and  $59 \pm 1$  Å, respectively.

*Unified Astronomy Thesaurus concepts:* Emission line galaxies (459); Cosmology (343); Galaxy evolution (594); Galaxy formation (595)

## 1. Introduction

The presence of significant Ly $\alpha$  emission in young, star-forming galaxies was first theorized by R. B. Partridge & P. J. E. Peebles (1967). Today, we understand Ly $\alpha$ -emitting galaxies (LAEs) as young, low-mass, low-dust, star-forming systems, which have been identified as predecessors of Milky

Way-type galaxies (e.g., E. Gawiser et al. 2007; L. Guaita et al. 2010; R. Pucha et al. 2022; J. P. Walker-Soler et al. 2012). LAEs have prominent Ly $\alpha$  emission due to the recombination of hydrogen in their interstellar media (ISM) and, in some cases, scattering that occurs in the circumgalactic medium (CGM). In the ISM, ionization is driven by active star formation (specifically hot young O-type and B-type stars; e.g., D. Kunth et al. 1998; L. Hui & N. Y. Gnedin 1997) or the presence of an active galactic nucleus (AGN) (e.g., H. Padmanabhan & A. Loeb 2021). After ionization via either of the aforementioned processes, the hydrogen undergoes recombination, producing



Original content from this work may be used under the terms of the [Creative Commons Attribution 4.0 licence](#). Any further distribution of this work must maintain attribution to the author(s) and the title of the work, journal citation and DOI.

$\text{Ly}\alpha$  radiation in significant quantities. Because LAEs are typically nearly dust-free (e.g., L. H. Weiss et al. 2021), the  $\text{Ly}\alpha$  emission line formed through these processes does not experience severe extinction from interstellar dust and stands out as a prominent spectral feature. In the range  $2 \lesssim z \lesssim 5$ , the expansion of the Universe redshifts this  $\text{Ly}\alpha$  emission-line feature from the rest-frame wavelength of 121.6 nm into the optical regime, making LAEs observable by ground-based telescopes.

After many years of unavailing searches for the fabled LAEs of R. B. Partridge & P. J. E. Peebles (1967), the development of more sensitive telescopes and wider-field detectors in the mid-1990s brought with it some of the first notable LAE surveys (see M. Ouchi et al. 2020 for a comprehensive review). One of the earliest successful LAE surveys was the Hawaii Survey, which used the 10 m Keck II Telescope to conduct narrowband and spectroscopic searches for high-EW LAEs at  $3 < z < 6$  (E. M. Hu et al. 1998). A few years later, the Large-Area Lyman Alpha survey used the CCD Mosaic camera at the 4 m Mayall telescope at Kitt Peak National Observatory and the low-resolution imaging spectrograph instrument at the Keck 10 m telescope to discover and spectroscopically confirm  $z = 4.5$  LAEs (J. E. Rhoads et al. 2000). Shortly thereafter, the Subaru Deep Survey was conducted using narrowband imaging at  $z = 4.86$  on the 8.2 m Subaru Telescope (M. Ouchi et al. 2003). Then, the Multiwavelength Survey by Yale–Chile (MUSYC) used the MOSAIC-II Camera at the Cerro Tololo Inter-American Observatory (CTIO) 4 m telescope (E. Gawiser et al. 2006b) to study LAEs at  $z = 2.1$  (L. Guaita et al. 2010) and  $z = 3.1$  (E. Gawiser et al. 2007). Subsequently, the Lyman Alpha Galaxies in the Epoch of Reionization (LAGER) Survey used the Dark Energy Camera (DECam) at the CTIO 4 m telescope to study cosmological reionization at  $z \sim 7$  (S. Harish et al. 2022; Z.-Y. Zheng et al. 2017). In recent years, the Hobby–Eberly Telescope Dark Energy Experiment (HETDEX) has taken the lead on spectroscopic LAE surveys (K. Gebhardt et al. 2021). Currently, the largest published narrowband-selected LAE samples have been discovered by the Systematic Identification of LAEs for Visible Exploration and Reionization Research Using Subaru HSC (SILVERRUSH), which used data from the Hyper Suprime-Cam (HSC) Subaru Strategic Program to discover LAEs over a wide range of redshifts (S. Kikuta et al. 2023; M. Ouchi et al. 2018).

Large, uniform samples of LAEs have a wide range of uses for studies of galaxy formation, galaxy evolution, large-scale structure, and cosmology. High-redshift LAEs ( $z \gtrsim 6$ ) can be used to probe the epoch of cosmic reionization, the era in which the neutral matter that existed after the recombination became ionized by first-generation stars (e.g., M. Ouchi et al. 2020; M. A. Schenker et al. 2014; D. P. Stark et al. 2010; C. C. Steidel et al. 1999; T. Yoshioka et al. 2022; Z.-Y. Zheng et al. 2017). Additionally, LAEs serve as good tracers of the large-scale structure of the Universe (e.g., A. Dey et al. 2016; Y. Huang et al. 2022; K. Shi et al. 2019), allowing us to study the temporal progression of the galaxy distribution at different epochs (e.g., E. Gawiser et al. 2007; K. Gebhardt et al. 2021). Since LAEs are composed of baryonic matter and dark matter halos, we can also use them as tools to measure the relationship between baryonic matter and dark matter, i.e., galaxy bias (A. L. Coil 2013). This type of analysis helps us to understand

how high-redshift galaxies grow into the systems we see today (e.g., E. Gawiser et al. 2007; L. Guaita et al. 2010; M. Ouchi et al. 2010). Lastly, we can use LAEs to study star formation histories by fitting their rest-ultraviolet through near-infrared photometry (V. Acquaviva et al. 2011; K. G. Iyer et al. 2019; K. Iyer & E. Gawiser 2017). This analysis allows us to characterize star formation episodes throughout the lifetime of galaxies, which can help us to better understand the physical processes that contribute to star formation and quenching in LAEs and how they compare to those in high-mass counterparts. Collectively, these scientific opportunities make LAEs a powerful observational tool for probing the high-redshift Universe, offering us many insights into the intricacies of galaxy formation and evolution, and cosmology. However, many of these studies require large, uniform samples of LAEs at well-separated periods in cosmological history.

One-hundred-deg<sup>2</sup> DECam Imaging in Narrowbands (ODIN) is a 2021–2024 NOIRLab survey program designed to discover LAEs using narrowband imaging (K.-S. Lee et al. 2023; V. Ramakrishnan et al. 2023). ODIN’s narrowband data are collected with DECam on the Víctor M. Blanco 4 m telescope at the CTIO in Chile. This project utilizes three custom-made narrowband filters with central wavelengths 419 nm (N419), 501 nm (N501), and 673 nm (N673) to create samples of LAE candidates during the period of Cosmic Noon at redshifts 2.4, 3.1, and 4.5, respectively. ODIN’s narrowband-selected LAEs allow us to view large snapshots of the Universe 2.8, 2.1, and 1.4 billion years after the Big Bang, respectively. With ODIN, we expect to discover a sample of  $>100,000$  LAEs in seven deep wide fields down to a magnitude of  $\sim 25.7$  AB, covering an area of  $\sim 100$  deg<sup>2</sup>. ODIN’s carefully chosen filters and unprecedented number of LAEs will enable us to create and validate samples of the galaxy population at three equally spaced eras in cosmological history. Using these data, we can trace the large-scale structure of the Universe, study the evolution of the galaxies’ dark matter halo masses, and investigate the star formation histories of individual LAEs.

In this paper, we introduce innovative techniques for selecting LAEs and reducing interloper contamination using ODIN data in the extended COSMOS field ( $\sim 9$  deg<sup>2</sup>), and introduce ODIN’s inaugural sample of  $\sim 17,000$  LAEs at  $z = 2.4$ , 3.1, and 4.5. By generating this unprecedentedly large sample of LAEs with impressive sample purity, ODIN will be able to better understand galaxy formation, galaxy evolution, and the large-scale structure of our Universe with significantly improved statistical robustness. From these results, we will be able to bind together chapters of the evolutionary biography of our Universe with what will be the largest sample of narrowband-selected LAEs to date.

In Section 2 we discuss the data acquisition and preprocessing. In Section 3 we introduce the hybrid-weighted double-broadband continuum estimation technique and selection criteria for our emission-line galaxy samples. In Section 4 we introduce our final emission-line galaxy samples and discuss their scaled median stacked spectral energy distributions (SEDs) and emission-line equivalent width distributions. In Section 5 we outline our conclusions and future work. Throughout this paper, we assume  $\Lambda$ CDM cosmology with  $h = 0.7$ ,  $\Omega_m = 0.27$ , and  $\Omega_\Lambda = 0.73$  and use comoving distance scales.

**Table 1**  
Filter Name, Effective Wavelength, FWHM, Seeing, Depth, and Extinction Coefficient ( $k$ ) for Each Filter in COSMOS (M. Sawicki et al. 2019; H. Aihara et al. 2019; K.-S. Lee et al. 2023)

Filter	$\lambda_{\text{eff}}$ (nm)	FWHM (nm)	Seeing (arcsec)	Depth (mag)	$k$
N419	419.3	7.5	1.1	25.5	3.64
N501	501.4	7.6	0.9	25.7	3.03
N673	675.0	10.0	1.0	25.9	2.01
$u$	368.2	86.8	0.92	27.7	4.06
$g$	481.1	139.5	0.74	27.8/28.4	3.17
$r$	622.3	150.3	0.79	27.4/28.0	2.28
$i$	767.5	157.4	0.57	27.1/27.7	1.61
$z$	890.8	76.6	0.75	26.6/27.1	1.24
$y$	978.5	78.3	0.73	25.6/26.6	1.09

## 2. Data

### 2.1. Images

For ODIN’s LAE selections, we require narrowband data as well as archival broadband data in the extended COSMOS field. The narrowband data for filters N419, N501, and N673 were collected using DECam on the Blanco 4 m telescope at CTIO by the ODIN team (K.-S. Lee et al. 2023). Archival *grizy* broadband data were acquired from the Hyper Suprime-Cam Subaru Strategic Program (HSC-SSP) (H. Aihara et al. 2019; S. Kawanomoto et al. 2018). HSC-SSP data were collected using the wide-field imaging camera on the prime focus of the 8.2 m Subaru telescope (H. Aihara et al. 2019). HSC-SSP imaging in the COSMOS field includes two layers, Deep and Ultradeep (H. Aihara et al. 2019). Archival broadband data for the  $u$  band were acquired from the CFHT Large Area  $u$ -band Deep Survey (CLAUDS; M. Sawicki et al. 2019). CLAUDS data were collected using the MegaCam mosaic imager on the Canada–France–Hawaii Telescope (CFHT; M. Sawicki et al. 2019) and covered a smaller area than the HSC-SSP. The effective wavelength, seeing, depth, and extinction coefficients (see Section 2.3) in the COSMOS field for each filter are presented in Table 1. The *grizy* seeing is reported as the median seeing value for each COSMOS wide-depth stack. Since the COSMOS field includes two layers for the HSC broadband data, we present the parameters for both the Deep and Ultradeep regions separated by a slash when necessary. The transmission curves for all of these filters are presented in Figure 1.

### 2.2. Source Extractor Catalogs

In order to carry out source detection, we first divide the narrowband stack into “tracts” to match the *grizy* images from the HSC-SSP (H. Aihara et al. 2019). Each tract spans an area of  $\sim 1.7 \times 1.7 \text{ deg}^2$ , with a small overlap between neighboring tracts. We select sources from each tract image separately using the Source Extractor (SE) software (E. Bertin & S. Arnouts 1996) run in dual image mode with one narrowband image as the detection band and the *grizy* plus remaining narrowband images as the measurement bands. This allows us to measure the source fluxes in identical apertures on all the frames. We measure the photometry in multiple closely spaced apertures, making it possible to interpolate the fractional flux enclosed within an aperture of any radius. While running SE, we filter each image with a Gaussian kernel with FWHM matched to the

narrowband point-spread function. We impose a detection threshold (DETECT\_THRESH) of  $0.95\sigma$ , where  $\sigma$  is the fluctuation in the sky value of the narrowband image, and a minimum area (DETECT\_MINAREA) of one pixel. These settings are optimized to detect faint point sources, which form the bulk of the LAE population. The specific value of DETECT\_THRESH is chosen to maximize the number of sources detected while still ensuring that the contamination of the source catalog by noise peaks remains below 1%. The extent of the contamination is estimated by running SE on a sky-subtracted and inverted (“negative”) version of the narrowband image. In this negative image, any true sources will be well below the detection threshold; any objects detected by SE are thus the result of sky fluctuations. So long as the sky fluctuations are Gaussian, i.e., the extent of the fluctuations above the mean is the same as that below, the number of sources detected in the negative image will be comparable to the number of false source selected with a given detection threshold.

The COSMOS/N419 SE catalog is presented in Figure 2. Note that this plot excludes regions where there is no overlap between the DECam and HSC-SSP/CLAUDS frames. After acquiring archival data and creating a source catalog, we carry out a series of steps related to data preprocessing, which are outlined in Sections 2.3–2.5.

### 2.3. Galactic Dust Corrections

As radiation from an extragalactic source travels through the Milky Way, it encounters dust clouds that cause absorption and scattering. As a consequence of this, the observed radiation from those sources appears to be dimmer and redder than the intrinsic radiation. In order to account for this effect and recover the intrinsic emission from the sources, we apply Galactic dust corrections to the data.

We estimate the amount of reddening that a source experiences by comparing its observed  $B - V$  color to its intrinsic  $B - V$  color, i.e.,  $E(B - V)$ . In order to calculate the  $E(B - V)$  value for each of our sources, we use the reddening map of D. J. Schlegel et al. (1998, hereafter SFD), as modified by E. F. Schlafly & D. P. Finkbeiner (2011), along with an E. L. Fitzpatrick (1999) reddening law. The resulting extinction coefficients for each filter, as interpolated from the DECam filter values presented by E. F. Schlafly & D. P. Finkbeiner (2011), are presented in Table 1.

To implement Galactic dust corrections, we apply the equation

$$\text{flux}_{\text{corr}} = \text{flux}_{\text{obs}} \times 10^{0.4kE(B-V)}, \quad (1)$$

where  $\text{flux}_{\text{corr}}$  represents the Galactic dust-corrected flux value,  $\text{flux}_{\text{obs}}$  represents the observed flux value,  $k$  represents the extinction coefficient for a particular filter, and  $E(B - V)$  represents the SFD reddening value for a particular source.

At this point, we reassign objects of low flux density ( $< 3.6 \times 10^{-7} \mu\text{Jy}$ ) a magnitude of 40 as a flag, which is intentionally chosen to be much dimmer than the main distribution of magnitudes (centered around 24 for the full sample).

### 2.4. Aperture Corrections for Photometry

To fully account for the intrinsic brightness of each source, it is imperative that we also apply aperture corrections to our

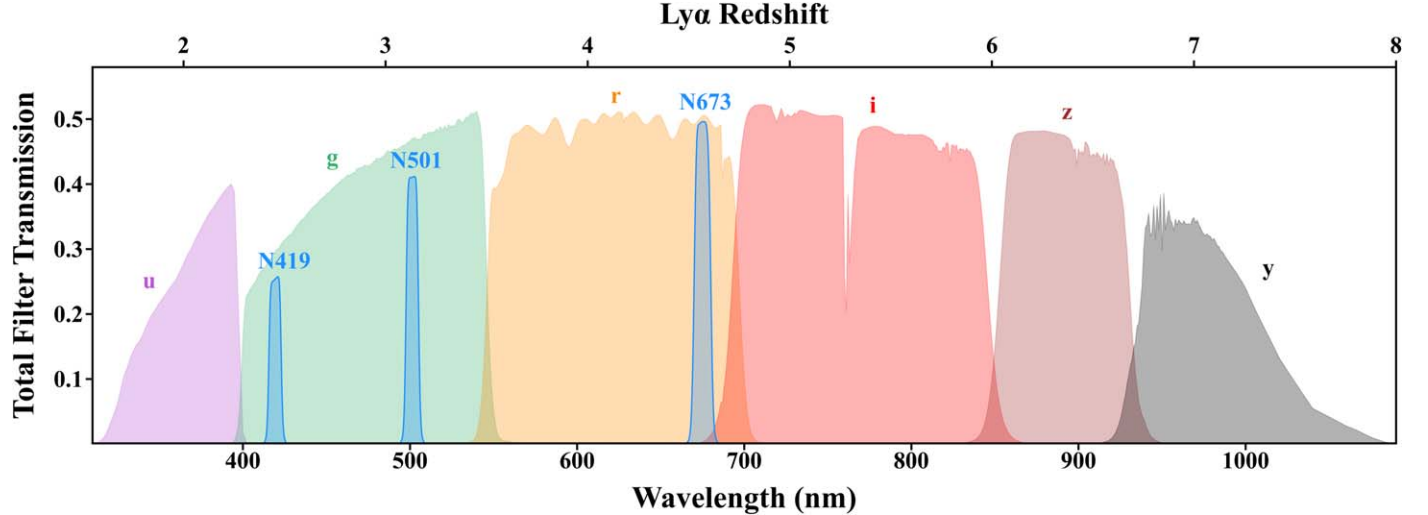


**Figure 1.** Filter transmission for N419, N501, N673,  $u$ ,  $g$ ,  $r$ ,  $i$ ,  $z$ , and  $y$ -band filters as a function of wavelength (bottom axis) and Ly $\alpha$  redshift (top axis). The  $u$ ,  $g$ ,  $r$ ,  $i$ , and  $z$ -band transmission curves are measured curves from CLAUDS and HSC (M. Sawicki et al. 2019; H. Aihara et al. 2019) while the N419, N501, and N673 transmission curves are simulated.

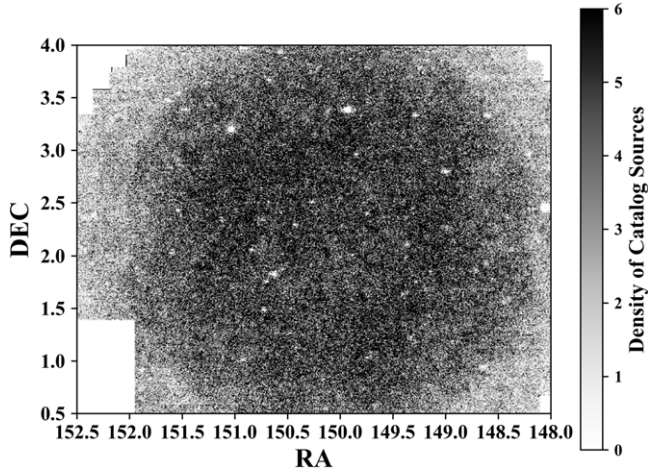


**Figure 2.** 2D histogram of the COSMOS/N419 Source Extractor catalog. The  $x$ -axis represents the R.A. in degrees and the  $y$ -axis represents the decl. in degrees. The color bar indicates the density of sources in each 2D bin. Only 9 deg $^2$  near the center, which has uniform depth, overlap with the HSC broadband data.

photometry. Each SE-generated source catalog produces flux density measurements for 12 different aperture diameters. Ideally, using the largest aperture available would yield the most accurate total flux measurements for the sources. However, by nature, the larger the aperture we use, the more noise is introduced by the background sky. On the other hand, if we use a smaller aperture we will underestimate the total flux densities of the sources but reduce the noise in our data. In order to accurately report the flux densities of our sources and limit the noise in the data, we use smaller apertures for the flux density measurements of the sources and apply correction factors to estimate the total flux density of a source in each filter. These flux density corrections are also carried through to the magnitude values and all errors. In order to properly treat point sources and extended sources, we use slightly different methodology for each class of objects.

To produce aperture correction factors for point sources, we examine the 2D integral of the point-spread function (which we will henceforth refer to as the Curve of Growth) for each filter

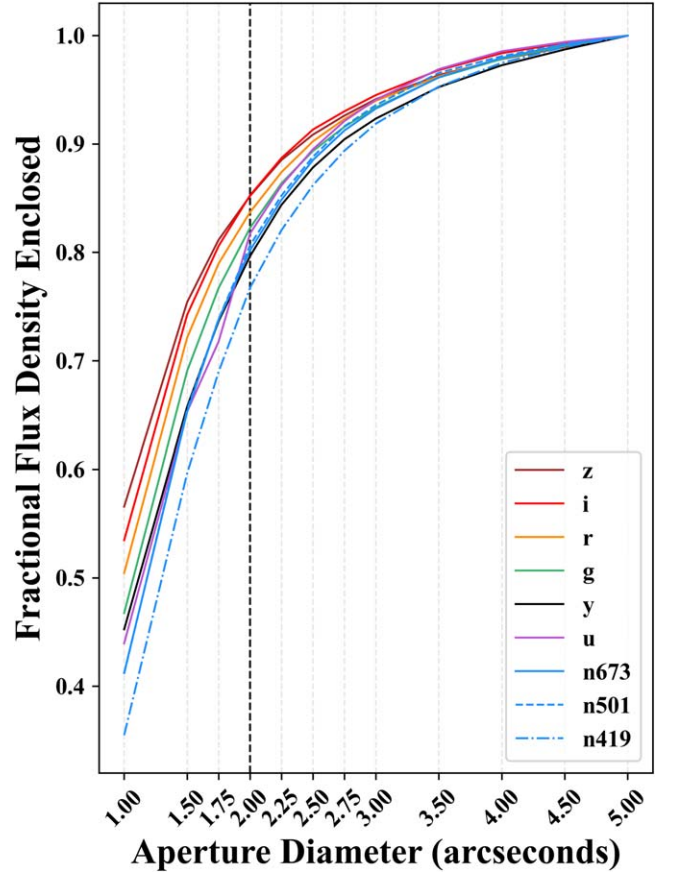


**Figure 3.** Curves of Growth for the  $u$ ,  $g$ ,  $r$ ,  $i$ ,  $z$ ,  $y$ , N419, N501, and N673 filters. The  $x$ -axis represents the aperture diameters in arcseconds and the  $y$ -axis represents the fractional flux density enclosed with respect to the largest aperture (5''.0 diameter). The darker vertical line corresponds to the chosen aperture diameter of 2''. The order of elements in the legend corresponds to the respective (vertical) fractional flux density in the 1'' aperture.

(see Figure 3). The Curves of Growth are constructed by plotting the median fractional flux density enclosed with respect to the largest aperture (5''.0 diameter),  $\text{fracflux}_n = f_n/f_5$ , for bright, unsaturated point sources as a function of aperture diameter for

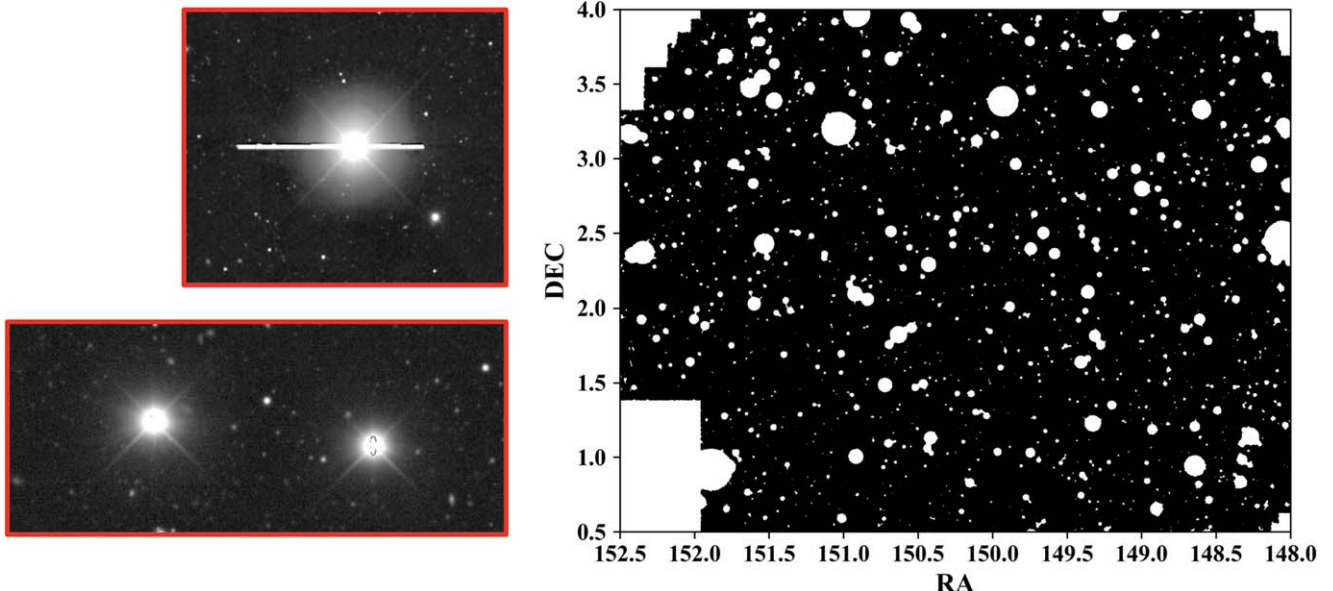


**Figure 4.** Representative example of starmasking to eliminate CCD blooming and saturated stars from COSMOS/N419. In the upper left and lower left panels, we present examples of CCD blooming and saturated stars in ODIN’s COSMOS/N419 images, respectively. In the right panel, the x-axis represents the R.A. in degrees and the y-axis represents the decl. in degrees. The sources that survive starmasking are presented in black.

each filter. We classify bright, unsaturated point sources as sources that obey the following criteria:

1. respective magnitude between 18 and 19 (bright),
2.  $\text{FLAGS} < 4$  (unsaturated),
3.  $\text{FLUX\_RADIUS} \leq 0.^{\circ}85$  (point source).

We choose the bright source magnitude range by finding the magnitudes for which the median fractional flux density levels out and the normalized median absolute deviation (NMAD) of the fractional flux density is close to zero in all filters. We choose to use the NMAD rather than the standard deviation because the NMAD is less sensitive to outliers. In order to omit sources with pixel saturation, we include only sources with the SE `FLAGS` parameter  $< 4$ . For the purpose of aperture corrections, we treat objects with a half-light radius (`FLUX_RADIUS`) less than or equal to  $0.^{\circ}85$  as point sources.

After creating Curves of Growth with the subset of sources that obey these criteria, we convert the median fractional flux density for a particular aperture into a correction factor for each filter,  $\text{corr} = 1/(\text{frac flux}_n)$ , such that  $\text{corr} \times f_n = f_5$ . The Curves of Growth for the COSMOS/N419 SE catalog are presented as a representative example in Figure 3. As a supplemental test of robustness, we also ensure that the Curve of Growth for each filter does not change dramatically across the survey area.

To produce aperture correction factors for extended sources, we perform a regression analysis to determine a correction factor as a function of source half-light radius in the chosen  $2''$  aperture for each filter. This step allows us to limit contamination from uncorrected extended sources in the candidate sample.

Ultimately, implementing these aperture corrections allows us to use a smaller aperture to better estimate the total flux of point sources without significantly biasing extended sources, while keeping the noise lower in the data. Additionally, at this step we apply a magnitude (flux) reassignment of 40 to sources whose flux values are low (including negative).

### 2.5. Starmasking

The next step in the candidate selection pipeline is starmasking. Starmasking removes data that have been contaminated by saturated stars and the effects of pixel oversaturation in the camera (CCD blooming). Starmasks were obtained from HSC-SSP (J. Coupon et al. 2018). We choose to use the *g*-band starmasks for this analysis because the individual masks were sufficiently sized for the narrowband images and did not have spurious objects. Examples of CCD blooming and saturated stars from the COSMOS/N419 sample as well as a visualization of the SE catalog after starmasking are presented in Figure 4 for reference.

### 2.6. Data Quality Cuts

At this point, we apply data quality cuts in order to eliminate any poor or problematic data that are not accounted for in the starmasks.

1.  $f_\nu \neq 0$ . We ensure that flux density  $f_\nu$  for each source is nonzero in the narrowband and broadband filters chosen for each LAE selection (see Sections 3.3–3.5 for details). This allows us to exclude sources with incomplete data.
2.  $S/N_{\text{NB}} \geq 5$ . We require that the narrowband signal-to-noise ratio (S/N) for a source is greater than or equal to 5, where the signal-to-noise ratio is taken as the ratio of the narrowband flux density and the narrowband flux density error. This eliminates sources that should not have entered the SE catalogs.
3.  $\text{IMAFLAGS\_ISO} = 0$ . We require that the SE parameter `IMAFLAGS_ISO` is equal to 0. `IMAFLAGS_ISO` is a binary parameter, so a value of 0 indicates that all the pixels within a source’s aperture have valid values and are unflagged, as opposed to a value of 1 indicating that any one pixel has no data or bad data in the external flag map (E. Bertin & S. Arnouts 1996).

4.  $\text{FLAGS} < 4$ . Lastly, we require that the SE FLAGS parameter is less than 4. This allows us to include sources whose aperture photometry is contaminated by neighboring sources and/or sources that had been deblended, and omit sources with pixel saturation (E. Bertin & S. Arnouts 1996).

### 3. Emission-line Galaxy Selection

#### 3.1. Improved Continuum Estimation Technique

By definition, a true LAE has excess Ly $\alpha$  emission when compared with expected continuum emission at the Ly $\alpha$  wavelength. In order to select LAE candidates, we utilize narrowband and broadband filters to infer the presence of an emission line at the redshifted Ly $\alpha$  wavelength by looking for excess flux density in the narrow band. In order to measure this excess, we use a narrowband filter to capture the Ly $\alpha$  emission line and two broadband filters to estimate the continuum emission at the narrowband effective wavelength. If a source's narrowband magnitude at this wavelength is significantly greater than the double-broadband continuum estimate, then the source is an LAE candidate.

We estimate the continuum at the narrowband wavelength using two broadband filters by generating a weight for each filter according to the equation

$$\lambda_{\text{NB}} = w\lambda_a + (1 - w)\lambda_b, \quad (2)$$

where  $\lambda$  represents the effective wavelength of a filter,  $w$  is a weight, NB represents the narrowband filter, and “ $a$ ” and “ $b$ ” generically represent two broadband filters. Since the effective wavelengths of each broadband filter are used to solve for  $w$ ,  $w$  will take on a value between 0 and 1 when used for an interpolation but can be outside that range when extrapolation is needed.

In order to use these weights to generate a double-broadband continuum estimation, we begin by making the realistic assumption that continuum-only sources have a power-law flux distribution. In practice, this allows us to compute the double-broadband magnitude by linearly weighting the magnitude from each broadband filter. This weighted magnitude model is presented in Equation (3), where  $\text{mag}_a$  is the magnitude in the “ $a$ ” broadband filter,  $\text{mag}_b$  is the magnitude in the “ $b$ ” broadband filter, and  $ab$  is the “ $ab$ ” double-broadband continuum magnitude at the effective wavelength of the narrowband:

$$ab = w \text{mag}_a + (1 - w)\text{mag}_b. \quad (3)$$

However, when the noise is a key contributor, magnitudes become too unstable to get a reliable fit. We remedy this issue by using a simpler model for the subset of sources with low S/N in the flux density (<10% of the starmasked source catalog). For this model, we assume that continuum-only sources' flux density has a linear relationship to wavelength (as used in E. Gawiser et al. 2006a). This weighted flux density model is presented in Equation (4), where  $f_a$  is the flux density in the “ $a$ ” broadband filter,  $f_b$  is the flux density in the “ $b$ ” broadband filter, and  $f_{ab}$  is the “ $ab$ ” double-broadband continuum flux density at the effective wavelength of the narrow band:

$$f_{ab} = wf_a + (1 - w)f_b. \quad (4)$$

We refer to this new method as hybrid-weighted double-broadband continuum estimation, in which we

1. treat sources with  $\text{S/N} \geq 3$  in both single broad bands by assuming a power-law flux density (i.e., weighted magnitude model; Equation (3));
2. treat sources with  $\text{S/N} < 3$  in either broad band by assuming a linear flux density (i.e., weighted flux model; Equation (4)).

For each sample, we use broad bands and weights  $w$  according to Table 2. After applying this method, we implement a global narrowband zero-point correction by adjusting the narrowband photometry such that the median narrowband excess is equal to zero for continuum-only objects. This correction is small and generally less than 10%.

This new method has many advantages for ODIN's data sets. First, it allows a better estimate the narrowband excess (equivalent width) of sources than is possible with a single broadband or flux-density-weighted double-broadband method. This is particularly advantageous for capturing dim LAEs. Additionally, it allows us to more effectively eliminate low-redshift interlopers from the high-redshift LAE candidates with minimal additional color cuts (see Sections 3.3 and 3.4). And lastly, it allows us to successfully use extrapolation (rather than interpolation) to estimate the continuum, which was not successful with a flux-density-weighted double-broadband method. This makes it possible to avoid direct use of the  $u$ -band filter for the  $z = 2.4$  LAE selection, which covers a smaller area and has more complex systematics than the  $g$  and  $r$  broadband filters (see Section 3.5). Therefore, the improved hybrid-weighted double-broadband continuum estimation technique allows us to reduce interloper contamination and select candidates over a larger area with more robust photometry.

#### 3.2. LAE Selection Criteria

Using hybrid-weighted double-broadband continuum estimation, we apply the following selection criteria to isolate LAEs:

1.  $ab - \text{NB} \geq (ab - \text{NB})_{\text{min}}$ . We require the narrowband excess of the LAE candidates to exceed an EW cut according to Equation (5), where  $\lambda_{\text{NB}}$  is the effective wavelength of the narrowband filter,  $\lambda_{\text{Ly}\alpha}$  is the minimum rest-frame wavelength of the Ly $\alpha$  emission line,  $\text{FWHM}_{\text{NB}}$  is the FWHM of the narrowband filter, and  $\text{EW}_0$  is the rest-frame equivalent width of the Ly $\alpha$  emission line (which we take to be 20 Å):

$$(ab - \text{NB})_{\text{min}} = 2.5 \log_{10} \left[ 1 + \text{EW}_0 \left( \frac{\lambda_{\text{NB}} / \lambda_{\text{Ly}\alpha}}{\text{FWHM}_{\text{NB}}} \right) \right]. \quad (5)$$

For the N419, N501, and N673 narrowband filters, this EW cut corresponds to narrowband excesses of 0.71, 0.83, and 0.82 mag, respectively. In Section 4.2, we will discuss a more complex process for estimation of equivalent width based on these values. This cut allows us to limit the number of low-redshift interlopers that have other emission lines in the narrowband filters. This cut is quite robust to small-EW interlopers, such as [O II]-emitting galaxies (R. Ciardullo et al. 2013), though some Green Pea-like [O III] emitters and AGNs may still remain in the sample (see Sections 3.3–3.5).

2.  $ab - \text{NB} \geq 3\sigma_{ab-\text{NB}}$ . We require that candidates have a robust narrowband excess in order to avoid continuum-only objects being included due to the photometric

**Table 2**

Double-broadband Filter Choices ( $a$  and  $b$ ) and Corresponding Weights ( $w$  and  $1 - w$ , Respectively) for Continuum Estimation at Each Narrowband Wavelength

Narrow Band	$a$	$w$	$b$	$1 - w$
N419	$r$	-0.438	$g$	1.438
N501	$g$	0.856	$r$	0.144
N673	$g$	0.323	$i$	0.677

uncertainties. Here,  $\sigma_{ab-\text{NB}}$  is calculated by propagating the errors in  $ab$  and NB.

3.  $\text{BB} - \text{NB} < -2.5 \log_{10} \left[ \frac{C_{\text{NB}}}{C_{\text{BB}}} \right] + 2\sigma_{\text{BB}-\text{NB}}$ . We require that an object is at least as bright in the emission-line-contributed broadband (BB) as a pure-emission-line LAE (infinite EW) would be, within  $2\sigma$  given possible noise fluctuations. Here,  $C$  is given by the equation

$$C = \frac{\int (c/\lambda^2) T d\lambda}{T_{\text{EL}}}, \quad (6)$$

where  $T$  is the filter transmission as a function of wavelength and  $T_{\text{EL}}$  is obtained by averaging the filter transmission over the narrowband filter transmission curve, which is used as a proxy for the LAE redshift probability distribution function.

4.  $R_{50} < 1.\text{''}38$ . We apply a cut in half-light radius  $R_{50}$  to exclude large, extended sources. We define this limit as twice the NMAD in the half-light radii for sources that satisfy the above criteria from the half-light radii of bright, unsaturated point sources. This allows us to eliminate highly extended low-redshift contaminants whose photometry is not sufficiently corrected to avoid spurious narrowband excess.
5.  $\text{NB} \geq 20$ . We exclude sources with narrowband magnitude brighter than 20 in order to eliminate extremely bright contaminants, typically quasars or saturated stars.
6.  $\text{NB} < D_{\text{NB},5\sigma}$ . We eliminate spurious objects whose narrowband magnitude is dimmer than the median  $5\sigma$  depth of the narrowband image  $D_{\text{NB},5\sigma}$ . For the N419, N501, and N673 narrowband filters, this magnitude corresponds to 25.5, 25.7, and 25.9 AB, respectively.
7.  $|f_{H1} - f_{H2}| < 3\sigma_{|f_{H1} - f_{H2}|}$ . We divide the individual narrowband images into two sets and use each to create a “half-stack.” We then eliminate objects whose flux density in these half-stacks ( $f_{H1}, f_{H2}$ ) shows a statistically significant difference, since such objects are likely spurious. We determine the uncertainty of this difference  $\sigma_{|f_{H1} - f_{H2}|}$  by summing the half-stack flux density errors in quadrature,  $\sqrt{\sigma_{H1}^2 + \sigma_{H2}^2}$ .

We also remove objects that appear in multiple LAE samples ( $\sim 1\%$ ), as these are likely to be bright low- $z$  interlopers such as AGNs. Finally, we apply additional color cuts to some of our LAE samples, which are designed to eliminate the largest known remaining sources of contamination in each data set and enhance the purity of our LAE samples. The sources of contamination and cuts as well as the double-broadband choices for each filter set are described below.

**Table 3**

LAE Selection Summary Statistics

LAE Redshift	2.4	3.1	4.5
Source extraction	1,083,476	1,482,315	2,535,478
Starmasking	868,184	1,199,385	2,077,563
Data quality cuts	558,908	747,466	1,209,843
LAE selection cuts	6100	5782	4870
Interloper rejection	6046	5694	4069
Specz rejection	6032	5691	4066
Final LAE sample	6032	5691	4066

### 3.3. Selection of $z = 4.5$ LAEs, $z = 0.81$ [O II] Emitters, and $z = 0.35$ [O III] Emitters

Out of the three samples of LAE candidates, the N673 catalog is the most susceptible to low-redshift emission-line galaxy interlopers. This is because the EW distributions and luminosity functions of low-redshift interlopers climb as a function of redshift. The two most notable interlopers are  $z \approx 0.81$  [O II] emitters and  $z \approx 0.35$  [O III] emitters, with the most challenging culprit being the [O III] emitters since the [O III] emission line(s) tend to have larger EWs than the [O II] emission line. We choose our selection filters specifically to isolate and remove these interlopers with minimal color cuts.

For our  $z = 4.5$  LAE selection, we carry out hybrid-weighted double-broadband continuum estimation using the N673,  $g$ -band, and  $i$ -band filters (see Section 3.4 and Table 3). Following Table 2, we define the double-broadband continuum estimation  $gi = 0.323g + 0.677i$ . This combination of filters has significant advantages over using just N673 and the  $r$  band. With the latter filter combination, not only do we have excess amounts of contamination from [O II] and [O III] emitters, but we do not capture all dim LAE candidates. Since N673 is the only one of our three narrowband filters for which it is feasible to perform interpolation between two broadband filters without either of them being affected by the Ly $\alpha$  emission line, we also explore this method. We find that excluding the  $r$ -band filter containing the emission line and instead using both the  $g$  band and  $i$  band increases the number of dim LAE candidates selected. We also find that this choice of filter reduces contamination from lower-EW [O II] emitters and that the majority of our resulting contamination is from Green Pea-like [O III] emitters (see Section 3.3). Green Pea galaxies are compact, extremely star-forming galaxies that are often thought of as low- $z$  LAE analogs (C. Cardamone et al. 2009).

In order to identify likely  $z = 0.81$  [O II] emitter and  $z = 0.35$  [O III] emitter interlopers in our data, we first carry out cross-matches between the SE source catalog and archival spectroscopic/photometric redshift catalogs as well as between the initial LAE candidate catalogs and archival spectroscopic/photometric redshift catalogs. We obtain archival spectroscopic redshift data from O. Le Fèvre et al. (2003, 2005, 2013), S. J. Lilly et al. (2007, 2009), B. Garilli et al. (2008), P. Cassata et al. (2011), A. L. Coil et al. (2011), G. B. Brammer et al. (2012), E. Bradshaw et al. (2013), R. J. Cool et al. (2013), R. McLure et al. (2013), R. E. Skelton et al. (2014), J. D. Silverman et al. (2015), D. T. Maltby et al. (2016), Kollmeier et al. (2017), M. J. Drinkwater et al. (2018), M. Scoggio et al. (2018), and D. Kashino et al. (2019), and we obtain photometric redshifts from J. R. Weaver et al. (2022).

As illustrated in Figure 5, we find that objects in our source catalog that are matched to low-redshift  $z = 0.81$  [O II] emitters

## [O II] Emitter Interlopers

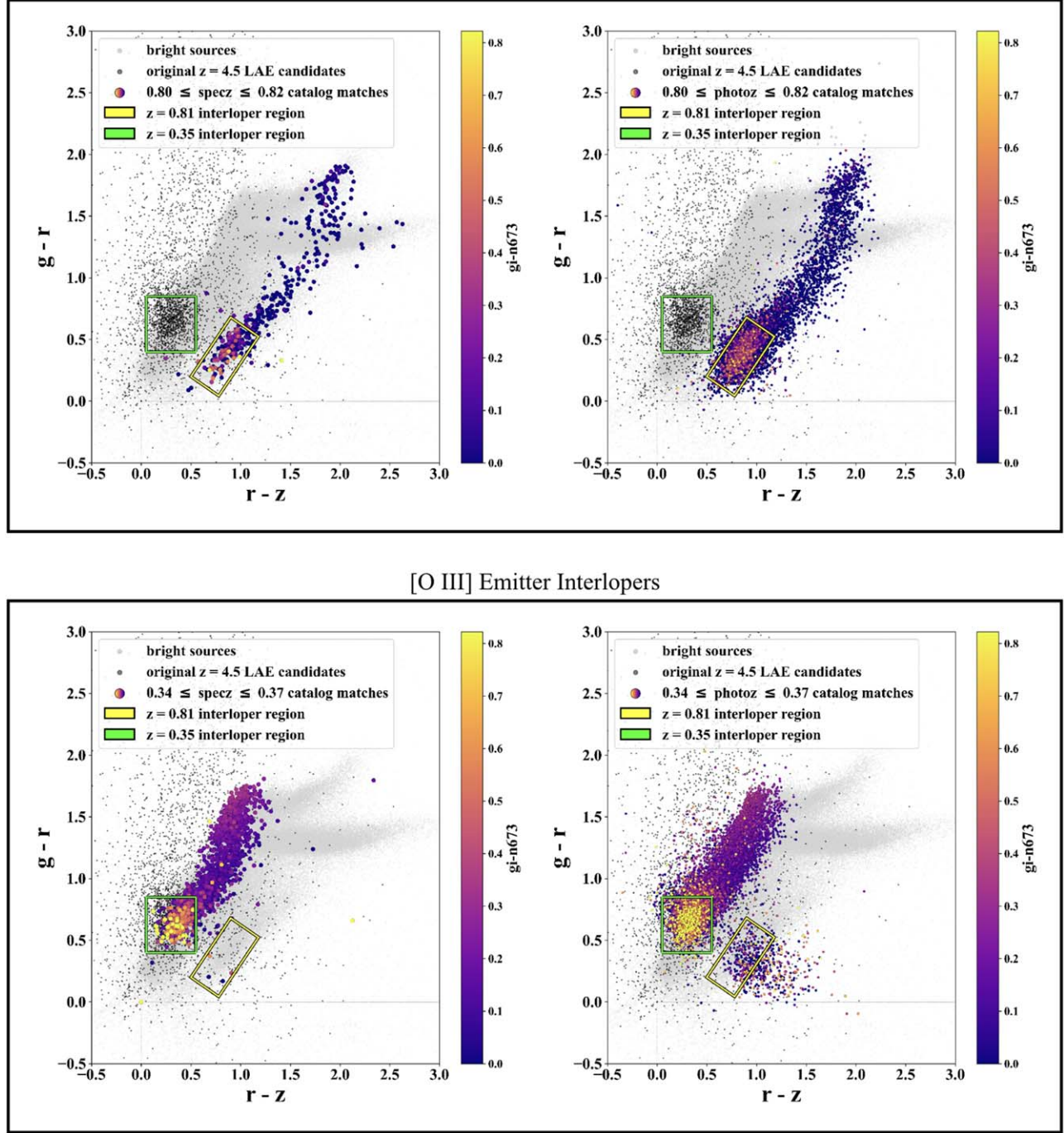


**Figure 5.**  $grz$  color-color diagrams demonstrating the compact, distinct regions in which [O II] and [O III] emitter interlopers reside. The top panel represents matches in the spectroscopic (left) and photometric (right) redshift source catalogs in the redshift range consistent with [O II] emitter interlopers. The bottom panel contains the equivalent diagrams for [O III] galaxies. The x-axis represents the difference between the  $r$ -band magnitude and the  $z$ -band magnitude, and the y-axis represents the difference between the  $g$ -band magnitude and the  $r$ -band magnitude. The light gray points represent bright objects in the SE source catalog. (Note that sources with a magnitude reassignment of 40 in at least two of the  $g$ ,  $r$ , and  $z$ -bands make up the light gray horizontal and vertical lines that intersect at  $(0, 0)$ . These particular objects are bright in the N673 narrow band, but have low flux in the  $g$ ,  $r$ , and  $z$ -bands.) The dark gray objects represent the original  $z = 4.5$  LAE candidates prior to interloper rejection. The color bar shows the coding for the  $(gi - N673)$  estimated EW of each cross-matched source. The yellow box shows the region of [O II] emitter selection, and the green box gives the locus of the [O III] emitters.

and  $z = 0.35$  [O III] emitters reside in specific, disjoint regions of  $grz$  color-color space. Furthermore, we find that the sources in these redshift ranges with higher estimated  $(gi - N673)$  equivalent widths occupy compact and distinct regions of  $grz$  color-color space. This can be seen in Figure 5, where the color bar displays the estimated narrowband excess from 0 to the

$z = 4.5$  LAE EW cutoff. In addition to examining the  $(gi - N673)$  excess of the objects, we also examine their  $(gr - N501)$  values (see Section 3.3.1). Examining both of these excesses is helpful because ODIN’s survey design ensures that the majority of  $z = 0.35$  galaxies emitting oxygen will have an [O III] emission line in the N673 filter and an [O II]

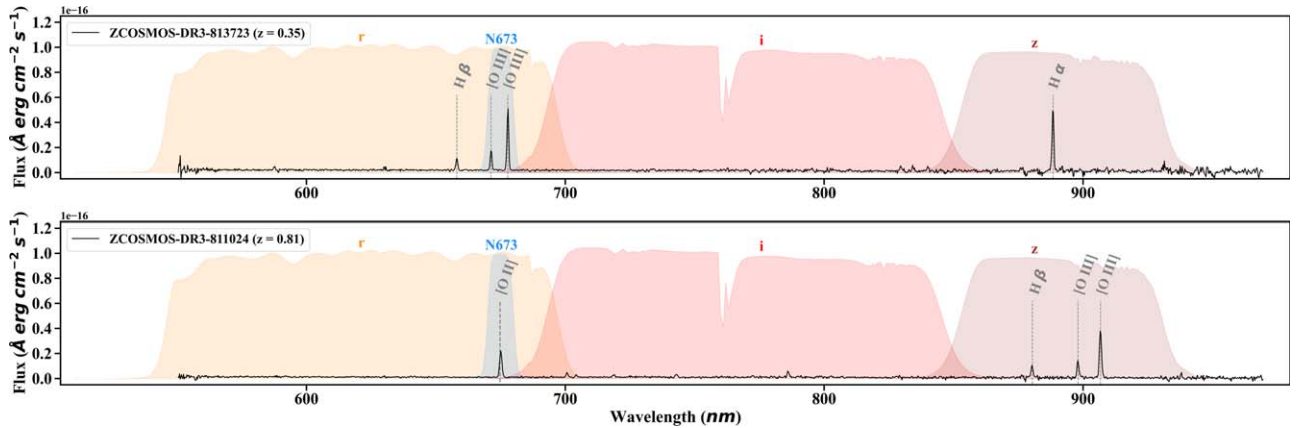


**Figure 6.** Examples of ODIN-selected low- $z$  emission-line galaxies superimposed on the filter transmission curves. The shaded curves represent the scaled filter transmission curves for the  $r$ ,  $i$ , and  $z$ -band filters. In the top panel, the black line represents the spectrum for the  $z = 0.35$  Green Pea-like galaxy ZCOSMOS-DR3-813723. The gray dashed vertical lines represent the expected locations of the  $H\beta$ ,  $[O\ III]$  doublet, and  $H\alpha$  lines. Although the ZCOSMOS spectrum does not extend to lower wavelengths, this object's  $[O\ II]$  emission line would fall within the N501 narrowband filter. In the bottom panel, the black line represents the spectrum for the  $z = 0.81$  galaxy ZCOSMOS-DR3-811024. The gray dashed vertical lines represent the expected locations of the  $[O\ II]$ ,  $H\beta$ , and  $[O\ III]$  doublet lines.

emission line in the N501 filter. We find that the objects with the highest ( $gr - N501$ ) color are also concentrated in the region where we predicted significant contamination from  $z = 0.35$  galaxies (see Section 3.3.1). This allows us to see that LAE selections at this redshift are strongly susceptible to  $z = 0.35$   $[O\ III]$  emitter interlopers and mildly susceptible to  $z = 0.81$   $[O\ II]$  emitter interlopers.

We also perform spectroscopic and photometric redshift cross-matches to our initial ( $gi - N673$ ) selected LAE candidates. The spectroscopic cross-match confirms that the primary contaminants in our LAE candidate sample lie within a redshift range consistent with  $z = 0.35$   $[O\ III]$  interlopers and in the region of our  $grz$  color–color diagram where we predicted  $z = 0.35$   $[O\ III]$  contamination. By visually inspecting the subset of these sources with accessible spectra (S. J. Lilly et al. 2007, 2009), we find that they have similar emission-line ratios to Green Pea-like  $z = 0.35$   $[O\ III]$  emitters (see Figure 6). Our photometric redshift cross-match also shows high levels of contamination from sources with redshifts that are consistent with  $z = 0.35$   $[O\ III]$  emitters in this same region in color–color space. Both cross-matches yield minimal contamination from sources with redshifts consistent with  $z = 0.81$   $[O\ II]$  emitters. However, we place less weight on conclusions drawn from photometric redshifts due to their susceptibility to misclassification of high-EW emission-line galaxies. These results suggest that  $z = 0.81$   $[O\ II]$  emitters and  $z = 0.35$   $[O\ III]$  emitters with high equivalent widths can be located in  $grz$  color–color space, eliminated from ODIN’s  $z = 4.5$  LAE sample, and set aside for independent analysis.

To further test our claims that the primary interloper contaminants in our sample of  $z = 4.5$  LAE candidates are Green Pea-like  $z = 0.35$   $[O\ III]$  emitters and that these interlopers preferentially reside in a specific region in  $grz$  color–color space, we plot confirmed Sloan Digital Sky Survey (SDSS) Green Peas in the appropriate redshift range (C. Cardamone et al. 2009). These Green Peas all have redshifts between 0.34 and 0.35 and correspond to objects with SDSS IDs 587732134315425958, 587739406242742472, and 587741600420003946 (C. Cardamone et al. 2009). To place these Green Pea-like  $[O\ III]$  emitters in  $grz$  color–color space, we run their SDSS spectra through ODIN’s filter set and obtain

the flux density in each filter. This is accomplished using Equation (7), where  $f_\nu$  is the flux density,  $S_\lambda$  is the galaxy’s spectrum,  $T$  is the filter transmission data,  $c$  is the speed of light, and  $\lambda$  is the wavelength:

$$f_\nu = \frac{1}{c} \frac{\int S_\lambda T \lambda \, d\lambda}{\int (T/\lambda) \, d\lambda}. \quad (7)$$

We carry out these calculations by numerically integrating using Simpson’s rule and then convert the flux density values  $f_\nu$  into AB magnitudes. We find that all of these SDSS Green Peas reside in the predicted region of  $grz$  color–color space (see Figure 7).

As an additional check, we perform a similar analysis with a simulated  $z = 0.35$  Green Pea-like galaxy spectrum and a simulated  $z = 0.81$   $[O\ II]$  emitter spectrum. We create these simulated spectra using the Flexible Stellar Population Synthesis (FSPS) package (C. Conroy et al. 2009; C. Conroy & J. E. Gunn 2010). For both simulations we use MESA Isochrones and Stellar Tracks (MIST; B. Paxton et al. 2011, 2013, 2015; J. Choi et al. 2016; A. Dotter 2016), the MILES spectral library (J. Falcón-Barroso et al. 2011), the DL07 dust emission library (B. Draine & A. Li 2007), a Salpeter initial mass function (IMF; E. E. Salpeter 1955), the Calzetti dust law (D. Calzetti et al. 2000), and turn on nebular emission and absorption in the intergalactic medium (IGM). Enabling nebular emission and IGM absorption tunes the stellar population to take on the properties of an observed galaxy. For the Green Pea-like galaxy, we also set the gas-phase metallicity and the stellar metallicity parameters to  $-1$ . This metallicity adjustment fine-tunes the relative emission-line strengths to match those of a typical Green Pea galaxy. For each spectrum, we compute the flux densities and AB magnitudes in ODIN’s filter set using Equation (7). We find that the simulated galaxies reside within both of their anticipated regions of  $grz$  color–color space (see Figure 7).

### 3.3.1. $[O\ II]$ and $[O\ III]$ Emitter Selection Criteria

Our analyses show that the regions in  $grz$  color–color space described in Section 3.3 are useful for targeting high-EW  $z = 0.35$   $[O\ III]$  emitter and  $z = 0.81$   $[O\ II]$  emitter interlopers in

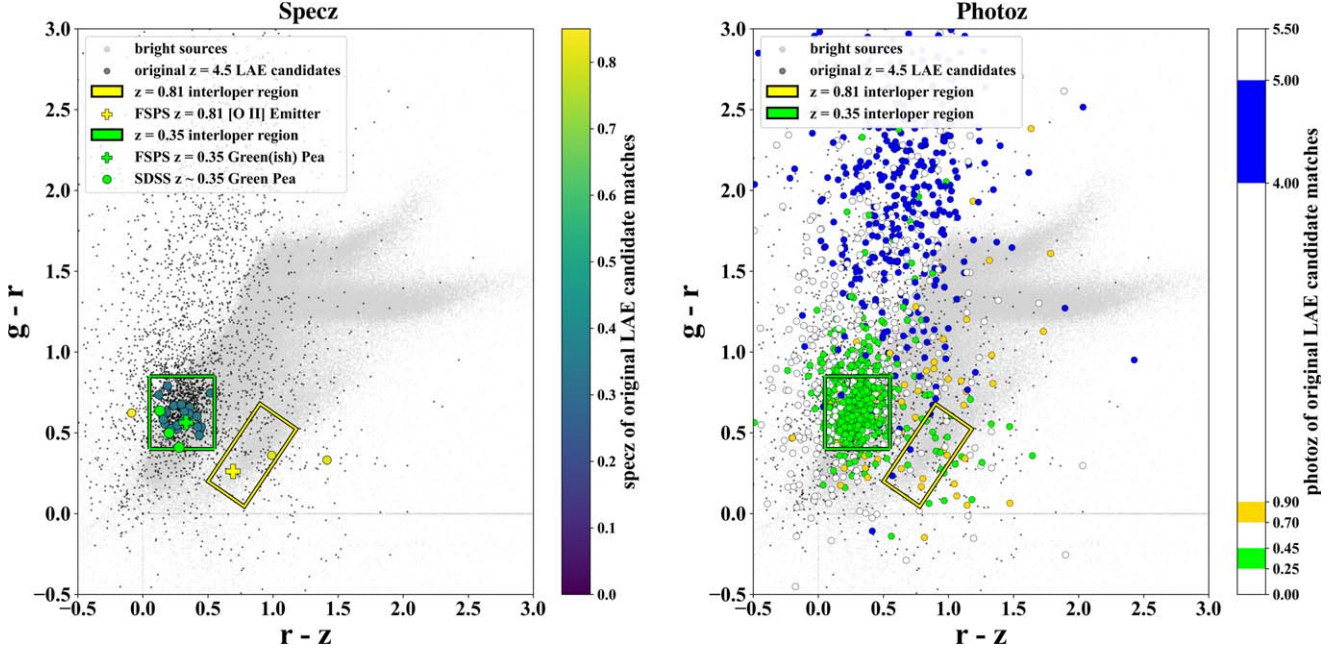


**Figure 7.**  $grz$  color–color diagrams demonstrating the distributions of spectroscopic and photometric redshift matches in the original  $z = 4.5$  LAE candidate list prior to interloper rejection. Also shown are the positions of simulated interlopers and SDSS Green Peas. The general format of these plots follows that of Figure 5. Here, the left panel introduces spectroscopic redshift matches in the original  $z = 4.5$  LAE candidate sample and the color bars give the redshift coding of the matched objects. Additionally, the yellow and green plus signs in the left panel show the positions of an FSPS simulated  $z = 0.81$  [O II] emitter and a  $z = 0.35$  Green Pea-like [O III] emitter, respectively (C. Conroy et al. 2009; C. Conroy & J. E. Gunn 2010). The green circles represent  $z \sim 0.35$  SDSS Green Peas (C. Cardamone et al. 2009). The right panel introduces photometric redshift matches in the original  $z = 4.5$  LAE candidate sample. The color bar distinguishes the redshift ranges corresponding to  $z = 0.35$  [O III] emitters (green),  $z = 0.81$  [O II] emitters (yellow), and  $z = 4.5$  LAEs (blue). These diagrams reveal the presence of significant contamination from  $z = 0.35$  [O III] emitters in the original  $z = 4.5$  LAE candidate sample.

our N673 data set. We can see that the choice to carry out a  $(gi - N673)$  LAE candidate selection yields a remarkably low level of contamination from  $z = 0.81$  [O II] emitters. These analyses also reveal that the most prominent source of contamination in the initial  $(gi - N673)$  LAE candidate sample is  $z = 0.35$  Green Pea-like [O III] emitters. This discovery allows us to apply a specific and minimal LAE selection cut in  $grz$  color–color space along with a  $(gr - N501)$  color excess criterion to eliminate bright  $z = 0.35$  emission-line galaxy interlopers (see Figure 8). These additional cuts not only significantly enhance the purity of our  $z = 4.5$  LAE sample, but also allow us to set aside this unique class of bright  $z = 0.35$  Green Pea-like [O III] emitters for future investigation. We therefore remove all sources that satisfy the additional criteria for our  $z = 4.5$  LAE candidate selection and reserve the sources that do satisfy the following criteria for an [O III] emitter candidate sample:

1.  $0.4 \leq g - r \leq 0.85$
2.  $0.05 \leq r - z \leq 0.55$
3.  $gr - N501 \geq 0.2$ .

At this point, we reject three additional spectroscopically confirmed low-redshift interlopers from our LAE sample with redshifts of 0.36, 0.37, and 0.80.

Supplementally, we can also generate a sample of  $z = 0.81$  [O II] emitter candidates by carrying out an  $(r - N673)$  selection and reserving objects that reside within the selected region in  $grz$  color–color space defined by the following criteria:

1.  $-0.89 \leq (g - r) - 1.2(r - z) \leq -0.40$
2.  $0.48 \leq (g - r) + 0.56(r - z) \leq 1.18$ .

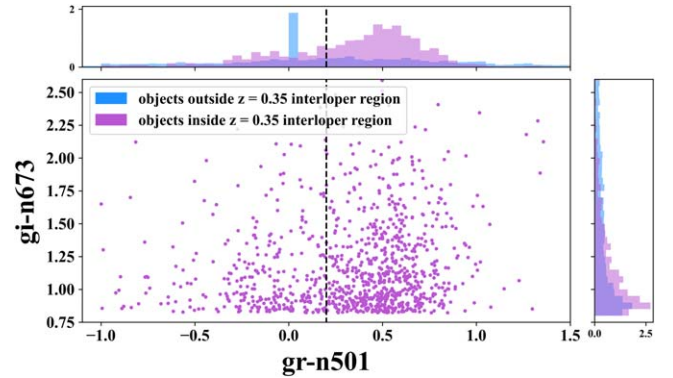


**Figure 8.** Scatter histogram illustrating  $z = 0.35$  Green Pea-like galaxy selection diagnostics. The central plot is a  $(gr - N501)$  vs.  $(gi - N673)$  color–color diagram of objects that passed our initial LAE selection criteria (see Section 3.2) and reside inside the  $grz z = 0.35$  interloper region (see Figures 5 and 7), shown in purple. The upper plot shows the  $(gr - N501)$  color distribution for candidates inside (purple) and outside (blue) the  $grz z = 0.35$  interloper region. (The peak in the blue histogram just above zero corresponds to relatively dim LAE candidates whose N501 flux is continuum-dominated.) The right plot shows the same for the  $(gi - N673)$  color. Each of the histograms is normalized such that its area sums to one. The dashed black vertical line shows the minimum N501 excess required for an object in the  $grz z = 0.35$  interloper region to be classified as a  $z = 0.35$  Green Pea-like galaxy and be eliminated from the  $z = 4.5$  LAE sample. Using the  $grz z = 0.35$  interloper region in tandem with this N673 and N501 narrowband excess diagnostic allows us to select a high-confidence sample of  $z = 0.35$  Green Pea-like interlopers without removing the natural scatter in N501 narrowband excess in the LAE sample.

### 3.4. Selection of $z = 3.1$ LAEs and $z = 0.35$ [O II] Emitters

For our  $z = 3.1$  LAE selection, we carry out hybrid-weighted double-broadband continuum estimation using the N501,

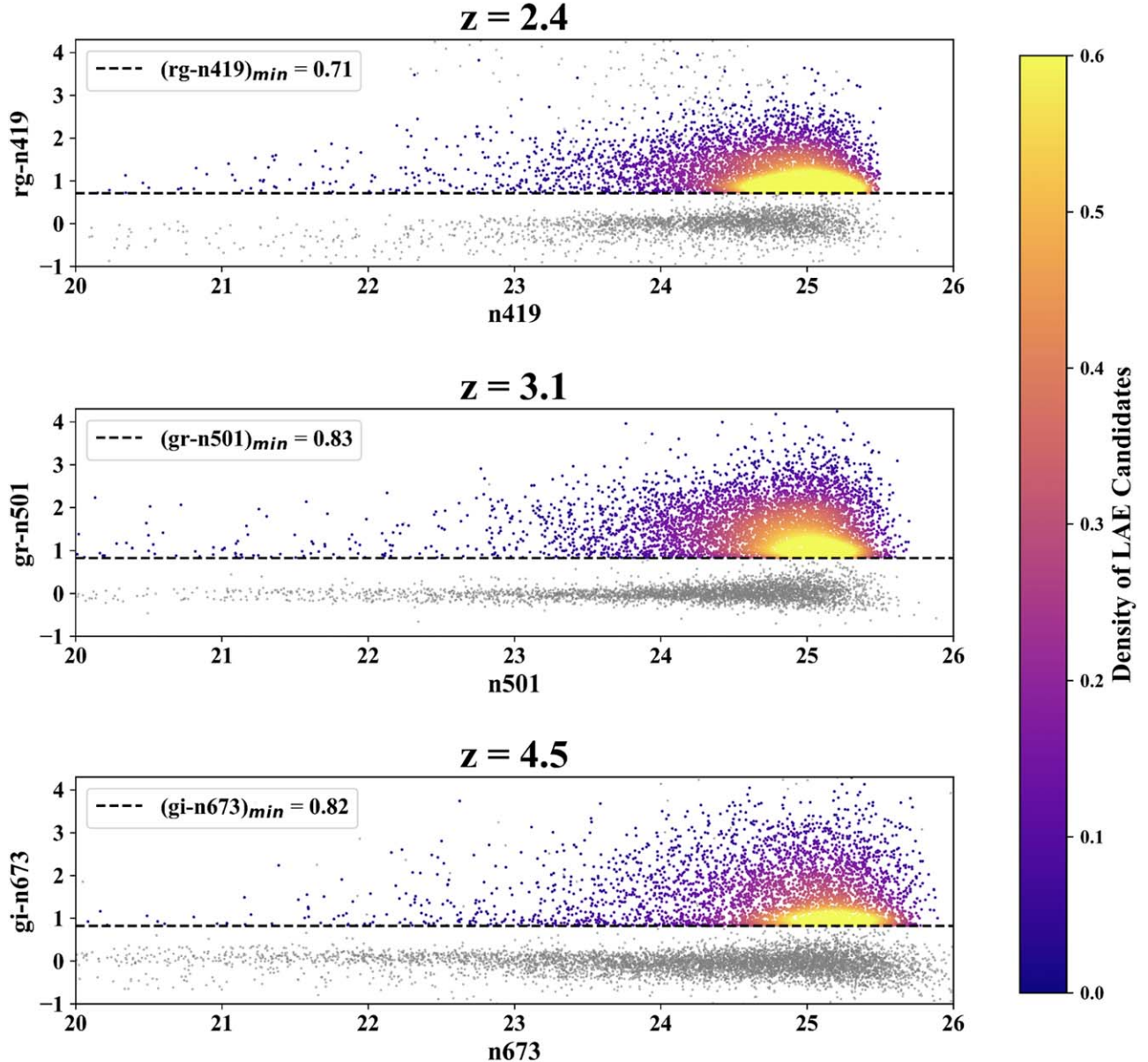


**Figure 9.** Color–magnitude LAE selection diagrams for  $z = 2.4$  (top),  $3.1$  (middle), and  $4.5$  (bottom). The  $x$ -axis represents the narrowband magnitude and the  $y$ -axis gives the narrowband excess as the difference between the double-broadband magnitude and the narrowband magnitude. The dashed line is the narrowband excess cut applied for each selection method. Random subsets of catalog sources are presented in gray. The color bar represents the density of LAEs in color–magnitude space.

*g*-band, and *r*-band filters (see Figure 9 and Table 3). Following Table 2, we define the double-broadband continuum estimation  $gr = 0.856g + 0.144r$ . Since the [O III] emission lines occur at rest-frame wavelengths of 495.9 nm and 500.7 nm, only very low- $z$  galaxies would have these emission lines at 501 nm. Because the EW distributions and luminosity functions of low-redshift interlopers are lower at lower redshift, low-redshift [O III] emitters do not pose a threat to the purity of our  $z = 3.1$  LAE sample. Additionally, due to their low redshifts, we expect most of these objects to be eliminated by the half-light radius cut. Therefore, the most likely source of low-redshift interloper contamination is  $z = 0.35$  [O II] emitters. That being said, the EW of the [O II] emission line tends to be significantly smaller than the corresponding [O III] EW and the typical Ly $\alpha$  EW.

In order to ensure that there is minimal contamination from  $z = 0.35$  [O II] emitters, we utilize the N673 narrowband filter,

which is designed to pick up the [O III] emission line for  $z = 0.35$  galaxies (as discussed in the previous subsection). We find that the  $(gi - N673)$  color for the  $z = 3.1$  LAE candidate sample is symmetrically distributed about a mean of  $-0.013$ . This shows that, as expected, if any [O II] contaminants do exist, they are not also bright in [O III]. We also find that the objects with higher  $(gi - N673)$  color for the original  $z = 3.1$  LAE candidate sample do not preferentially reside in the region of  $grz$  color–color space where we have previously identified the population of  $z = 0.35$  [O III] emitters in our N673-detected LAE sample. These conclusions imply that our LAE candidate sample does not contain noticeable contamination from  $z = 0.35$  [O II] emitters, which is consistent with previous results from C. Gronwall et al. (2007). Lastly, we remove three spectroscopically confirmed low-redshift interlopers from our LAE sample with redshifts 0.82, 2.10, and 2.14. We also confirm two LAE redshifts.

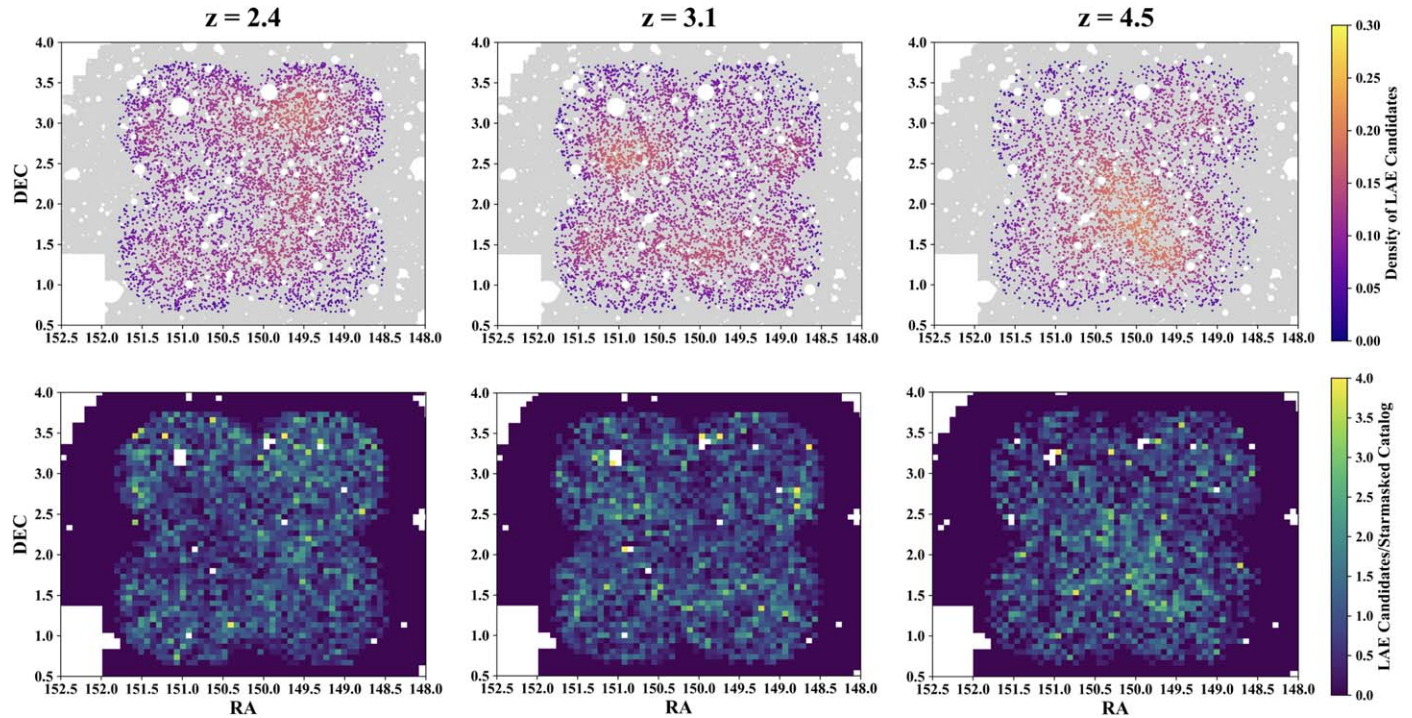


**Figure 10.** Spatial distributions of  $z = 2.4$  (left),  $3.1$  (middle), and  $4.5$  (right) LAE samples. The  $x$ -axis represents the R.A. in degrees and the  $y$ -axis represents the decl. in degrees for all panels. In the top three panels, the catalog sources are presented in gray and the LAE densities are represented by a Gaussian kernel density estimator and the color bar. The bottom three panels are 2D histograms that represent the relative spatial distribution of LAEs. The color bar demonstrates the ratio of LAE density to that of sources in the starmasked catalog, scaled to the average ratio in each data set.

### 3.5. Selection of $z = 2.4$ LAEs

For our  $z = 2.4$  LAE selection, we carry out hybrid-weighted double-broadband continuum estimation using the N419,  $g$ -band, and  $r$ -band filters (see Figure 9 and Table 3). Following Table 2, we define the double-broadband continuum estimation  $rg = -0.438r + 1.438g$ . Rather than using broadband filters on either side of the narrowband filter to estimate our continuum (i.e.,  $u$  band and  $r$  band), we choose to use the  $g$  and  $r$  broadband filters to define the galactic continua. This is advantageous because it makes it possible to select  $z = 2.4$  LAE candidates without direct use of the  $u$ -band filter, which is shallower than the  $g$ - and  $r$ -band filters. This choice is also beneficial because the  $u$ -band data cover a smaller area than the  $g$  and  $r$  bands, and are plagued by more systematic issues than the  $g$  and  $r$  bands.

Out of our three LAE candidate samples, the  $z = 2.4$  LAE sample using our N419 filter is the least susceptible to low-redshift emission-line galaxy interlopers (with the exception of inevitable narrow and broad emission-line AGNs). It is nonetheless important to complete a thorough spectroscopic follow-up on this candidate sample to fully assess its purity. Lastly, we reject 14 spectroscopically confirmed low-redshift interlopers from our LAE sample with redshifts 0.13, 0.13, 0.22, 0.79, 0.83, 0.88, 0.93, 1.02, 1.03, 1.16, 1.2, 1.35, 1.68, and 1.72. We also confirm seven LAE redshifts.

## 4. Results

Using our selection criteria, we find samples of 6032  $z = 2.4$  LAEs, 5691  $z = 3.1$  LAEs, and 4066  $z = 4.5$  LAEs in the extended COSMOS field ( $\sim 9 \text{ deg}^2$ ;  $\sim 7.8 \text{ deg}^2$  post-starmasking). The number of candidates remaining after each step in the LAE selection pipeline is presented in Table 3. The samples

correspond to LAE densities of 0.21, 0.20, and 0.14  $\text{arcmin}^{-2}$ , respectively. We also find that there are 665  $z = 0.35$  [O III] emitters and 375  $z = 0.81$  [O II] emitters. There are eight specz matches in the  $z = 0.35$  [O III] emitter catalog and there is 1 specz match in the  $z = 0.81$  [O II] emitter catalog. All of these specz matches are in the corresponding redshift ranges. We present the color–magnitude LAE selection diagrams for all three redshifts in Figure 9, where the LAEs are displayed in color and a subsample of random field objects are shown in gray. We present the spatial distribution of LAEs in each sample in Figure 10. The latter plots show that there are no pronounced systematic effects impacting our LAE selection as a function of spatial position at any of the three redshifts. The overdense regions in these figures also suggest that there are unique structures in the LAE candidate populations, providing the starting point for a subsequent clustering analysis (D. Herrera et al. 2024, in preparation).

### 4.1. Scaled Median Stacked SEDs

SED stacking is a technique used to represent generalized characteristics for a sample of objects. When creating a stacked SED, it is assumed that all galaxies in the sample have similar physical properties and that the properties of the stacked SED will match the physical properties of typical individual galaxies. As a consequence of this, every stacking method has the limitation that it cannot capture the diverse properties in a galaxy sample. However, SED stacking can be a helpful tool for understanding sample purity, especially for objects with faint continuum emission and expected continuum breaks such as LAEs.

There are two primary classes of stacking: image stacking and flux stacking. Within each of these classes, there are three predominant stacking methods: mean, median, and scaled

median. Mean stacking yields a good representative value if there are no outliers in the sample, but the result can be skewed if there is a wide spread in galaxy characteristics or contamination from AGNs or low- $z$  interlopers. Median stacking has less susceptibility to outliers and contaminants, but does not take into account the spectral shapes of all objects in a sample and is relatively inefficient. C. J. Vargas et al. (2014) showed that the best simple stacking method for representing SED properties of  $z = 2.1$  LAEs is scaled median stacking, which has the added advantage that the influence of overall brightness variations is removed. In this study we choose to follow in the footsteps of C. J. Vargas et al. (2014) and use flux-scaled median stacking for our population SEDs. We outline the procedure for this method below.

In order to create scaled median stacked SEDs, we first find the median of the flux densities in our scaling filter  $\tilde{f}_{\text{scale}}$ . Then, we create a scaling factor for each source  $\delta_i$  by computing the ratio of the median flux density in our scaling filter  $\tilde{f}_{\text{scale}}$  to the flux density measurement for each source in our scaling filter  $f_{\text{scale},i}$ :

$$\delta_i = \tilde{f}_{\text{scale}} / f_{\text{scale},i}. \quad (8)$$

Next, we calculate the scaled flux density of a filter  $[F_{\text{filt}}]$  by multiplying the flux density measurements in that filter  $f_{\text{filt},i}$  by the scaling factor  $\delta_i$ .

$$[F_{\text{filt},i}] = f_{\text{filt},i} \times \delta_i. \quad (9)$$

Lastly, we use the median of the scaled flux density for all sources in the filter to determine the filter's scaled median stacked flux density  $\tilde{F}_{\text{filt}}$ . By following this prescription for all of our filters, we create a scaled median stacked SED for each LAE sample.

In addition to carrying out scaled median stacking, we also create median stacked and mean stacked SEDs for comparison. We find that the mean stacked SED yields flux densities that are much larger than for our (scaled) median stacked SEDs. This confirms that mean stacking is highly susceptible to outliers and brightness variations in our LAE sample. In contrast, we find that our scaled median stacked SEDs and our median stacked SEDs do not yield drastically different results, though our scaled median stacked SEDs have smaller interquartile ranges. We also find that our scaled median stacked SEDs are robust to changes in the scaling filter for all filters except for the  $u$  band. This is not surprising. At  $z = 3.1$  and  $4.5$ , the  $u$  filter's bandpass lies partially or entirely blueward of the Lyman break, and even at  $z = 2.4$ , the flux recorded by the filter is strongly affected by the Ly $\alpha$  forest. Large stochastic differences in  $u$ -band flux are therefore expected (e.g., B. Venemans et al. 2005; P. Madau 1995).

We present the results of these stacked LAEs in color-magnitude space in Figure 11;  $u$ -band data have been excluded for the aforementioned reasons. Although Figure 11 only shows the results for the  $z = 2.4$  LAEs, the behavior is similar across all three redshifts. Overall, we find that the standard deviation in narrowband magnitude for the narrowband,  $g$ ,  $r$ ,  $i$ ,  $z$ , and  $y$  scaled median stacked LAEs is  $0.04 \pm 0.01$  mag and the standard deviation in scaled median ( $ab - NB$ ) color is  $0.02 \pm 0.02$ . The agreement among these values argues that our scaled median stacking methods are robust. These results also reinforce the conclusion that scaled median stacking is a defensible method for this analysis.

To form our LAE SEDs, we began by normalizing each galaxy's flux density to its measurement in the  $i$  band; this filter does not contain a Ly $\alpha$  emission line nor any other strong spectral line feature at  $z = 0.35$ ,  $0.81$ ,  $2.4$ ,  $3.1$ , or  $4.5$ , and its use minimizes the interquartile ranges for our flux density values. Additionally, we exclude objects with  $i$ -band magnitude  $\geq 40$  (the low-flux density flag) from our SEDs since their small scaling factor causes the scaled flux densities of the other filters to become artificially inflated. We also do not include objects with no  $u$ -band data from the  $u$ -band stacks since the  $u$  band covers a smaller area than the HSC filters used in the selection process.

We can assess the overall success of our LAE selection by examining the stacked SEDs. In Figure 12, we present the  $i$ -band scaled median stacked SEDs for the  $z = 2.4$ ,  $3.1$ , and  $4.5$  LAE candidate samples. These SEDs contain the key features that we expect to find in LAE spectra. First, there is clear evidence for absorption by the Ly $\alpha$  forest in all three SEDs. The Ly $\alpha$  forest is characterized by absorption from hydrogen gas clouds in between the observer and the galaxy. This absorption occurs from the Ly $\alpha$  line down to shorter wavelengths, so we expect the Ly $\alpha$  forest decrement to occur most distinctly in the broad band whose effective wavelength is immediately below the effective wavelength of the corresponding narrow band. Our SEDs reveal that the Ly $\alpha$  forest decrement is present in the  $u$  band for  $z = 2.4$ , in N419 at  $z = 3.1$ , and in the  $r$  band at  $z = 4.5$ . We do not see a clear decrement in the  $g$  band for the  $z = 3.1$  SED because in this case the  $g$  band also includes the Ly $\alpha$  emission line. We also find that the Lyman break is present in our SEDs. The Lyman break is characterized by the complete absorption of ionizing photons by gas below the short-wavelength end of the Lyman series transitions, the Lyman limit. In the rest frame, this limit corresponds to 91.2 nm. At a redshift of  $2.4$ , we expect the Lyman limit to occur at  $\sim 310$  nm. Because this wavelength falls out of the transmission ranges of our broadband filters, we do not see evidence for (or against) the Lyman limit in our  $z = 2.4$  LAE candidate SED. At a redshift of  $3.1$ , we expect the Lyman limit to occur at  $\sim 374$  nm. This is close to both the effective wavelength and long-wavelength limit of the  $u$  band (see Table 1). We see a strong effect from the Lyman break in the  $u$  band for our  $z = 3.1$  LAE SED. For the redshift  $4.5$  LAEs, we expect to find the Lyman limit at  $\sim 502$  nm. This is  $\sim 20$  nm longer than the effective wavelength and  $\sim 50$  nm shorter than the long-wavelength limit of the  $g$  band (see Table 1). Therefore, in the  $g$  band, N419, and N501 we see the partial effect of the Lyman break, and in the  $u$  band we see its full effect. Across the three redshifts, the strong presence of the Ly $\alpha$  forest decrement and the Lyman break suggests the general success of our LAE selections.

In Figure 13, we also present the  $i$ -band scaled median stacked SEDs for the  $z = 0.35$  [O III] emitters,  $z = 0.81$  [O II] emitters, and  $z = 4.5$  LAEs. Since all of these samples were selected from the N673-detected SE catalog, comparing them offers valuable insight into the success of our interloper rejection/selection methods. We find that the  $z = 0.35$  [O III] emitters and the  $z = 0.81$  [O II] emitters are generally much brighter in the  $i$  band than  $z = 4.5$  LAEs; this is consistent with their much smaller luminosity distances. Additionally, the  $z = 0.35$  [O III] emitters have significant flux density in the N501 filter due to the presence of the redshifted [O II] emission. Furthermore, we find that the Green Pea-like galaxies have

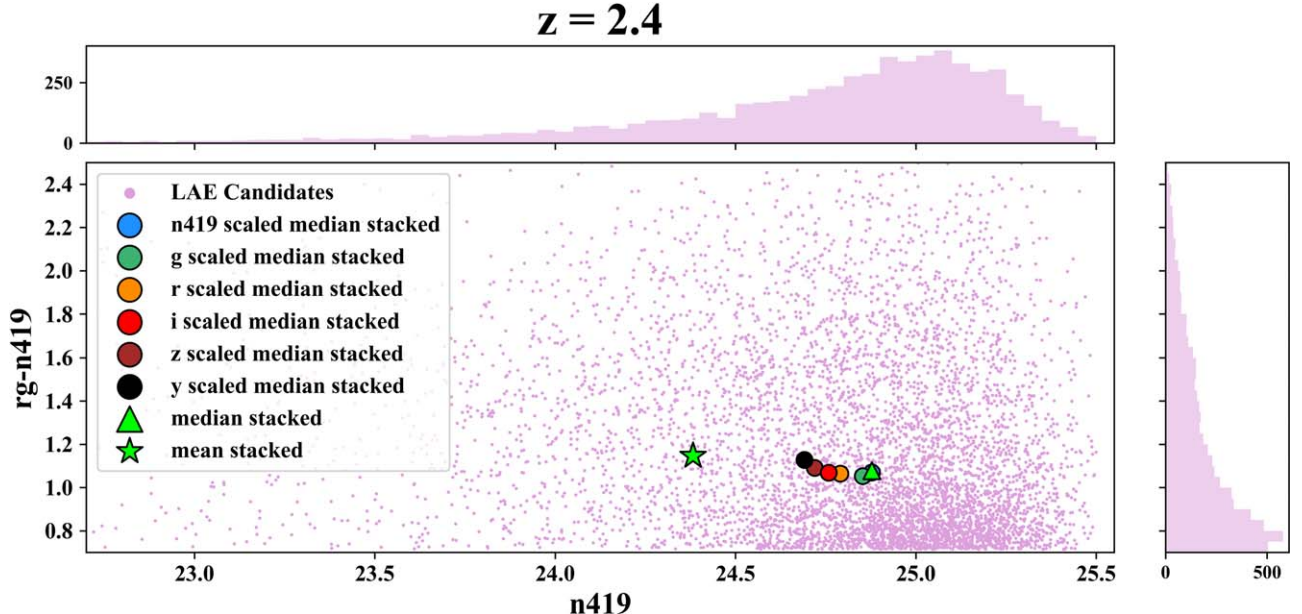


**Figure 11.** Color-magnitude scatter histogram for comparison of SED stacking methods using the  $z = 2.4$  LAE sample. The  $x$ -axis represents the N419 narrowband magnitude and the  $y$ -axis represents the narrowband excess. The light pink represents the  $z = 2.4$  LAEs, the colored circles represent the scaled median stacked LAEs, the green triangle represents the median stacked LAE, and the green star represents the mean stacked LAE in color-color space. The order of the circular points on the plot matches the legend from right to left. This figure demonstrates the general robustness of the scaled median stacking method and reinforces the conclusion that, of the three methods, this is the optimal stacking method for this analysis.

heightened flux density in the  $r$  band due to the presence of the  $H\beta$ ,  $[O\text{ III}] \lambda 4959$ , and  $[O\text{ III}] \lambda 5007$  emission lines and in the  $z$  band due to the presence of the  $H\alpha$  emission line (see Figure 6). Similarly, the  $z = 0.81$   $[O\text{ II}]$  emitter systems have an excess of flux density in the  $z$ -band due to the presence of the  $H\beta$ ,  $[O\text{ III}] \lambda 4959$ , and  $[O\text{ III}] \lambda 5007$  emission lines (see Figure 6). Lastly, we find that both the  $z = 0.35$   $[O\text{ III}]$  emitters and the  $z = 0.81$   $[O\text{ II}]$  emitters have significant emission in the  $g$  band and  $u$  band, whereas the  $z = 4.5$  LAEs exhibit the presence of a partial and full Lyman break in these filters. These features imply that our rejection/selection methods for low-redshift emission-line interlopers are successful.

#### 4.2. Ly $\alpha$ Equivalent Width Distributions

Now that we have shown our LAE samples have high levels of purity, we can use them to quantify the Ly $\alpha$  EW distribution at each redshift. We define the EW as the width of a rectangle from zero intensity to the continuum level with the same area as the area of the emission line. Physically, the Ly $\alpha$  EW is related to the burstiness of LAEs since it compares the Ly $\alpha$  emission from O and B stars to the continuum emission from O, B, and A stars (with radiative transfer) (A. Broussard et al. 2019). Therefore, quantifying the Ly $\alpha$  EW distribution is helpful for comparing sample characteristics of LAEs.

We derive the rest-frame Ly $\alpha$  EW distribution for each LAE sample following the methodologies of B. Venemans et al. (2005) and L. Guaita et al. (2010). For a detailed derivation, see the Appendix of L. Guaita et al. (2010).

First, we take the rest-frame equivalent width as  $EW_{\text{obs}}/(1+z)$ , where the observed equivalent width  $EW_{\text{obs}}$  is defined as follows:

$$EW_{\text{obs}} = A/B, \quad (10)$$

where  $A$  and  $B$  are defined in Equations (11) and (12):

$$A = Q_{\text{NB}} - Q_{ab} 10^{(ab-\text{NB})/2.5} \quad (11)$$

$$B = \frac{w_{\text{BB}} T_{\text{EL,BB}}(c/\lambda_{\text{EL}}^2) 10^{(ab-\text{NB})/2.5}}{\int (c/\lambda^2) T_{\text{BB}}(\lambda) d\lambda} - \frac{T_{\text{EL,NB}}(c/\lambda_{\text{EL}}^2)}{\int (c/\lambda^2) T_{\text{NB}}(\lambda) d\lambda}. \quad (12)$$

In Equation (11),  $Q$  is the fraction of the continuum flux in a particular filter that is transmitted by the Ly $\alpha$  forest,  $ab$  is the double-broadband magnitude, and NB is the narrowband magnitude. We define  $Q$  using the equation

$$Q_{\text{filt}} = \frac{\int e^{-\tau_{\text{eff}}(\lambda)} (c/\lambda^2) T(\lambda) d\lambda}{\int (c/\lambda^2) T(\lambda) d\lambda}, \quad (13)$$

where  $T(\lambda)$  is the filter transmission at a given wavelength and  $\tau_{\text{eff}}(\lambda)$  is the effective opacity of H I. For this analysis, we use Equation (14) as an approximation for all observed wavelengths below the redshifted Ly $\alpha$  line (W. Press et al. 1993; B. Venemans et al. 2005; P. Madau 1995):

$$\tau_{\text{eff}}(\lambda) = 0.0036 \left( \frac{\lambda}{1216 \text{ \AA}} \right)^{3.46}. \quad (14)$$

In Equation (12), BB refers to the selection broad band that also has a flux contribution from the emission line, and  $w_{\text{BB}}$  is the weight assigned to that broad band. For the  $(rg - \text{N419}) z = 2.4$  LAE selection and the  $(gr - \text{N419}) z = 3.1$  LAE selection, this broad band corresponds to the  $g$  band. In the case of the  $(gi - \text{N673}) z = 4.5$  LAE selection, neither of the broadband filters has a flux contribution from the emission line, so the first term in Equation (12) vanishes entirely.  $T_{\text{EL}}$  is obtained by averaging the filter transmission over the narrowband filter transmission curve, which is used as a proxy for the LAE redshift probability distribution function. This is justifiable

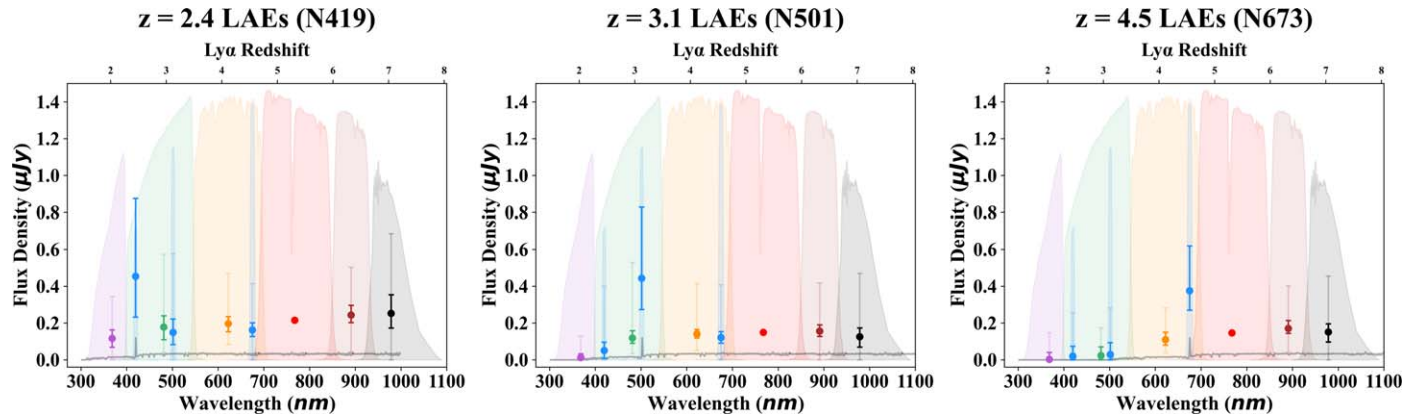


**Figure 12.**  $i$ -band scaled median stacked spectral energy distributions for the LAE samples at  $z = 2.4$  (left),  $3.1$  (middle), and  $4.5$  (right). The lower  $x$ -axis represents the wavelength in nanometers, the upper  $x$ -axis represents the the Ly $\alpha$  redshift, and the  $y$ -axis represents the flux density in microjanskys. From left to right, the shaded curves represent the filter transmission for  $u$ ,  $g$ ,  $r$ ,  $i$ ,  $z$ , and  $y$  broadband filters. The subplots also include filter transmission curves for N419, N501, and N673 narrowband filters, respectively. All the filter transmission curves have been scaled to fit the  $y$ -axis range of the flux density data. The  $i$ -band scaled median stacked flux density for each filter is plotted at the effective wavelength of the corresponding filter. The translucent error bars represent the 50% confidence intervals and the opaque error bars represent the 95% confidence intervals. (The  $i$  band has no error bars since all data are scaled to this filter.) The subplots also include grayscaled LAE spectra as an aid to interpretation. The LAE spectra were adapted from A. E. Shapley et al. (2003). The strong presence of the Ly $\alpha$  forest decrement and the Lyman break in these SEDs suggests the success of our LAE candidate selection methods in achieving high sample purity.

since the filter transmission curve is close to a top hat.  $\lambda_{\text{EL}}$  is the wavelength corresponding to the emission line, i.e., the narrowband effective wavelength.

We fit the resulting Ly $\alpha$  EW distributions using an exponential distribution as shown in Equation (15) and a Gaussian distribution as shown in Equation (16), where  $N$  is the number of LAEs in a given EW bin,  $C$  is a constant of the fit, EW is the rest-frame Ly $\alpha$  EW, and  $w_0$  and  $\sigma_{\text{gauss}}$  are the respective scale lengths in angstroms:

$$N = C \exp\left(\frac{-\text{EW}}{w_0}\right) \quad (15)$$

$$N = C \exp\left(\frac{-\text{EW}^2}{2\sigma_{\text{gauss}}^2}\right). \quad (16)$$

We present these Ly $\alpha$  EW distributions and fits for the  $z = 2.4$ ,  $3.1$ , and  $4.5$  LAE samples in Figure 14. To obtain a robust fit, we choose to clip our distributions at a minimum EW of  $40 \text{ \AA}$ . We also choose to exclude objects with EW above  $400 \text{ \AA}$  since the highest equivalent widths are associated with galaxies that are extremely faint in the continuum, and thus poorly measured. This results in the exclusion of less than 1% of our LAE sample. Lastly, we choose to use 200 bins for the fits, corresponding to the minimum bin number for which the scale lengths for all three data sets become stable. We find that the exponential scale lengths for the three LAE samples are  $w_0 = 53 \pm 1$ ,  $65 \pm 1$ , and  $59 \pm 1 \text{ \AA}$ ; and the Gaussian scale lengths are  $\sigma_{\text{gauss}} = 72 \pm 1$ ,  $87 \pm 2$ , and  $79 \pm 2 \text{ \AA}$ , respectively. The reduced  $\chi^2$  values for the exponential scale lengths are 1.9, 1.1, and 1.3; and the reduced  $\chi^2$  values for the Gaussian scale lengths are 3.9, 2.6, and 2.3, respectively. The reduced  $\chi^2$  values unanimously show preference toward an exponential fit when compared to a Gaussian fit. Although there is significant variation in the literature results, the  $w_0$  scale lengths are similar to previous findings and the  $\sigma_{\text{gauss}}$  are between  $\sim 10\%$  and  $40\%$  lower than most previous findings (e.g., C. Gronwall et al. 2007; M. Ouchi et al. 2008; K. K. Nilsson et al. 2009; L. Guaita

et al. 2010; R. Ciardullo et al. 2011; J. Kerutt et al. 2022). Contamination from low-redshift emission-line or continuum-only galaxies tends to reduce the scale length; contamination from spurious objects tends to increase them, since the EWs are formally infinite when an “object” is only luminous in the narrow band. We have made a careful effort to avoid all of these types of contamination, with our stacked SED analysis providing evidence against significant low-redshift contamination. Our finding that the EW scale length is at the lower end of results in the literature might indicate that we are free from significant contamination from spurious objects. However, it is possible that these results are impacted by selection effects. For example, some studies have shown that excluding objects with fainter UV continuum can result in smaller scale lengths (e.g., T. Hashimoto et al. 2017; G. A. Oyarzún et al. 2017). Obtaining a better understanding of contamination rates and sample characteristics from each type of interloper will further improve the accuracy of these measurements. Additionally, the full ODIN LAE sample should result in even more precise measurements of the Ly $\alpha$  EW distributions.

#### 4.3. LAEs with Measured $\text{EW} \geq 240 \text{ \AA}$

Additionally, we investigate the objects with  $\text{EW} \geq 240 \text{ \AA}$ . It has been speculated that a real LAE with EW in this regime could have a normal stellar population with a clumpy dust distribution or could be composed of young, massive, metal-poor stars or Population III stars; however, measurements of the short-lived He II  $\lambda 1640$  line and C IV  $\lambda 1549$  render the true composition of these systems ambiguous (N. Kashikawa et al. 2012). We find that there are 484, 561, and 245 LAEs in this regime at  $z = 2.4$ ,  $3.1$ , and  $4.5$ , respectively.

We seek to understand the likelihood that these objects are real and are not the result of noise. In order to accomplish this, we first truncate our EW distributions at  $240 \text{ \AA}$  and forward-model the scatter in our data using a bootstrapping method to see how many objects exceed an EW of  $240 \text{ \AA}$ . We accomplish this by taking each observed object with  $\text{EW} < 240 \text{ \AA}$  and applying random values within  $1\sigma$  of that object’s noise in the

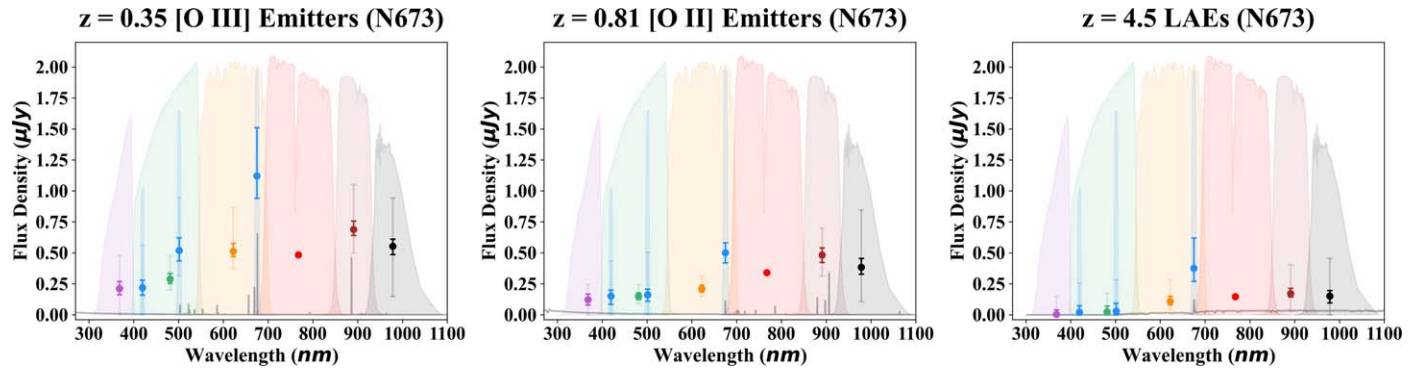


**Figure 13.** *i*-band scaled median stacked spectral energy distributions for the N673-selected line emitters, namely the  $z = 0.35$  [O III] emitter sample (left),  $z = 0.81$  [O II] emitter sample (middle), and  $z = 4.5$  LAE sample (right). The template of these plots follows Figure 12. [O III] and [O II] emitter spectra were generated using FSPS (C. Conroy et al. 2009; C. Conroy & J. E. Gunn 2010), and the LAE spectrum was adapted from A. E. Shapley et al. (2003). The lack of evidence for the Ly $\alpha$  forest decrement and the Lyman break in the [O III] emitter and [O II] emitter SEDs suggests that these populations are not dominated by  $z = 4.5$  LAEs. Additionally, the elevated flux density in bands containing emission lines in the [O III] emitter and [O II] emitter spectra suggests that these populations are dominated by [O III] emitters and [O II] emitters, respectively.

double-broadband magnitude and in the narrowband magnitude, then recalculating EW. We then carry out this process multiple times until the average fraction of objects above  $240\text{ \AA}$  converges. Using this method, we find that  $10_{-0.5}^{+0.4}\%$ ,  $31_{-0.3}^{+2}\%$ , and  $191_{-5}^{+1}\%$  of the objects above  $240\text{ \AA}$  can be explained by noise, respectively. However, we find that objects with  $\text{EW} \geq 240\text{ \AA}$  tend to have higher noise in their double-broadband magnitudes than objects with  $\text{EW} < 240\text{ \AA}$ . In order to account for this, we apply a similar noisification method where we instead take each observed object with  $\text{EW} < 240\text{ \AA}$  and apply random noise values from the high-EW sample to the double-broadband magnitude and the narrowband magnitude, then recalculate EW. Using this method, we find that  $102_{-4}^{+0.2}\%$ ,  $85_{-0.05}^{+4}\%$ , and  $411_{-8}^{+1}\%$  of the objects above  $240\text{ \AA}$  can be explained by noise, respectively. Although the bootstrapping method suggests that there may be objects with truly high EW in the  $z = 2.4$  and  $3.1$  samples, the latter method implies that the high-EW objects might be explained by the large fraction of the sample that is formally undetected in the broadband imaging, leading to large uncertainties in EW. Additionally, we carry out Gaussian error propagation and find that only 1.0%, 1.2%, and 1.2% of these high-EW objects have measured rest-frame  $\text{EW} > 240\text{ \AA}$  at  $3\sigma$  significance, respectively. Follow-up spectroscopy of this subset will be a priority to better understand how many of these objects truly have  $\text{EW} \geq 240\text{ \AA}$ .

## 5. Conclusions and Future Work

ODIN is a NOIRLab survey program designed to discover LAEs by combining data taken through three narrowband filters custom-made for the Blanco 4 m telescope’s DECam imager (K.-S. Lee et al. 2023) with archival broadband data from the HSC and CLAUDS. ODIN’s narrowband filters, N419, N501, and N673, allow us to identify samples of LAEs at redshifts 2.4, 3.1, and 4.5, corresponding to epochs 2.8, 2.1, and 1.4 Gyr after the Big Bang, respectively. When the ODIN survey is complete, we expect to discover  $>100,000$  LAEs in seven of the deepest wide-imaging fields up to a narrowband magnitude of  $\sim 25.7$  AB, covering an area of  $\sim 100\text{ deg}^2$ .

In this paper, we used data from ODIN’s first completed field covering  $\sim 9\text{ deg}^2$  in COSMOS to introduce innovative techniques for selecting LAEs and other samples of emission-line galaxies using narrowband imaging. These include LAE samples at  $z = 2.4$ ,  $3.1$ , and  $4.5$ , as well as samples of  $z = 0.35$

[O III] emitters and  $z = 0.81$  [O II] emitters. The main conclusions of this work are summarized below:

1. We developed a narrowband LAE selection method that utilizes a new technique to estimate emission line strength, the hybrid-weighted double-broadband continuum estimation technique. Using this technique, we treated sources with  $\text{S/N} \geq 3$  in both single broadbands by assuming a power-law SED and treated sources with  $\text{S/N} < 3$  in either broadband by assuming a linear spectral slope. This technique allowed us to better estimate expected continuum emission at the location of each narrowband filter by utilizing data from any two nearby broadbands. This method provided the flexibility to choose optimal broadband filters that maximize the data area and quality and to avoid broadbands that may be heavily impacted by features in low-redshift emission-line interlopers.
2. Utilizing this new technique, we performed  $z = 2.4$ ,  $3.1$ , and  $4.5$  LAE candidate selections in the extended COSMOS field using broadband data from the HSC and narrowband data collected with DECam. We used the N419, *r*, and *g* bands for our initial  $z = 2.4$  LAE selection; the N501, *g*, and *r* bands for our initial  $z = 3.1$  LAE selection; and the N673, *g*, and *i* bands for our initial  $z = 4.5$  LAE selection.
3. We found that the main source of low-redshift emission-line contamination in our LAE samples was very bright  $z = 0.35$  Green Pea-like galaxies. Our data also revealed that these galaxies occupy a compact and distinct region of *grz* color–color space. Moreover, since the ODIN survey was designed in anticipation of  $z = 0.35$  contaminants, the filter bandpasses were designed to ensure that the majority of  $z = 0.35$  emission-line galaxies will have [O III] emission in the N673 narrowband filter and [O II] emission in the N501 narrowband filter. Despite having emission lines detectable in both the N673 and the N501 narrowband filters, our results suggested that these  $z = 0.35$  bright Green Pea-like galaxies are only a strong source of contamination in our N673  $z = 4.5$  LAE selection. By taking advantage of the *grz* color criteria and the estimated N673 and N501 excess flux densities, we were able to identify and set aside a sample of 665  $z = 0.35$  Green Pea-like objects for further analysis.

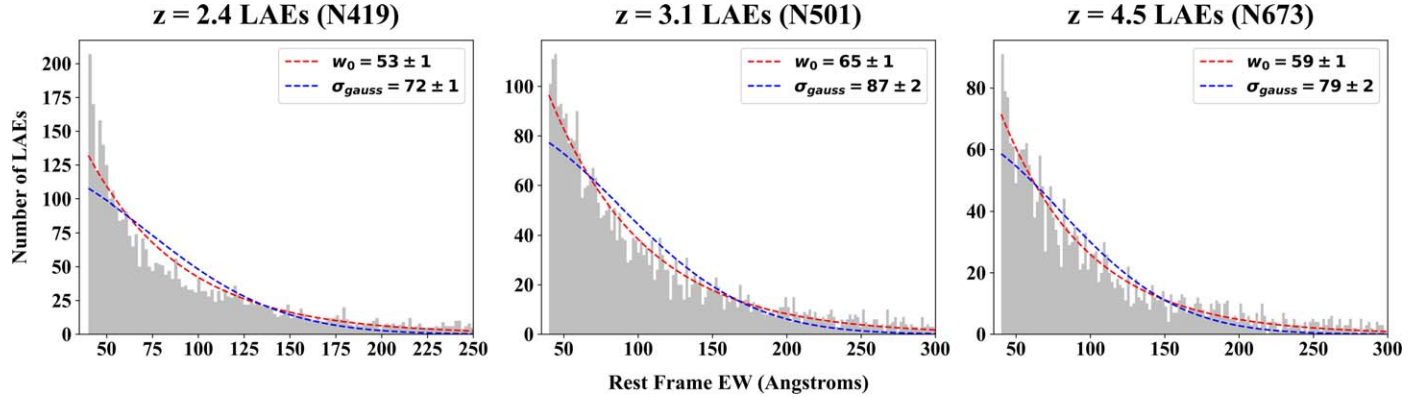


**Figure 14.** Rest-frame Ly $\alpha$  equivalent width distributions for  $z = 2.4$  (left),  $3.1$  (middle), and  $4.5$  (right) LAE samples. The  $x$ -axis represents the rest-frame Ly $\alpha$  EW in angstroms and the  $y$ -axis represents the number of LAEs in a given EW bin. A histogram of the EW distribution for each sample is presented in gray. The scale length for an exponential fit  $w_0$  to each distribution is presented in angstroms with a red dashed line. The scale length for a Gaussian fit  $\sigma_{\text{gauss}}$  to each distribution is presented in angstroms with a blue dashed line. These results suggest an evolution in scale length with increasing redshift.

Although we did not find that  $z = 0.81$  [O II] emitters are a notable source of contamination in our  $z = 4.5$  LAE candidate sample, we found that they also occupy a compact and distinct region of  $grz$  color–color space and are selectable using the N673 and  $r$ -band filters. Thus, we also set aside a sample of  $z = 0.81$  [O II] emitter galaxies for future analysis.

4. We found that there are 6032, 5691, and 4066 LAEs at  $z = 2.4$ ,  $3.1$ , and  $4.5$ , respectively, in the extended COSMOS field ( $\sim 9$  deg $^2$ ). The samples imply LAE surface densities of  $0.21$ ,  $0.20$ , and  $0.14$  arcmin $^{-2}$ , respectively. These results were in agreement with the predictions outlined in K.-S. Lee et al. (2023). We also defined samples of 665  $z = 0.35$  Green Pea-like galaxies and 375  $z = 0.81$  [O II] emitters.
5. We developed  $i$ -band flux density scaled median stacked SEDs for the  $z = 2.4$ ,  $3.1$ , and  $4.5$  LAE samples as well as the  $z = 0.35$  Green Pea-like [O III] emitter and  $z = 0.81$  [O II] emitter galaxy contaminants. We found that our  $z = 2.4$ ,  $3.1$ , and  $4.5$  LAE SEDs display clear features that are unique to LAEs such as the Ly $\alpha$  forest decrement and Lyman break. We found that our  $z = 0.35$  Green Pea-like [O III] emitter and  $z = 0.81$  [O II] emitter SEDs have features unique to their respective populations. Our stacked SEDs revealed broad consistency in each sample, implying that our samples have high levels of purity.
6. We calculated Ly $\alpha$  equivalent width distributions for the  $z = 2.4$ ,  $3.1$ , and  $4.5$  LAE samples. We found that the EW distributions are best fit by exponential functions with scale lengths of  $w_0 = 53 \pm 1$ ,  $65 \pm 1$ , and  $59 \pm 1$  Å, respectively. These scale lengths are at the lower end of the values reported in the literature. The precision of these measurements should improve for the considerably larger LAE sample expected from the full ODIN survey.
7. We found that an impressive  $\sim 10\%$  of our LAE samples have measured rest-frame equivalent width  $\geq 240$  Å, providing possible evidence of nonstandard IMFs or clumpy dust. However, deep spectroscopic follow-up is needed to ascertain how many of these equivalent widths are real as opposed to noise due to low continuum S/N.

ODIN’s LAE samples will allow us to quantify the temporal evolution of LAE clustering properties, bias, dark matter halo masses, and halo occupation fractions (D. Herrera et al., in

preparation). As HETDEX and DESI-II work to probe dark energy using LAEs, ODIN’s improved understanding of which dark matter halos host LAEs can allow these groups to better simulate their systematics, and will have a direct impact on their measurements of cosmological constraints. Furthermore, ODIN’s LAE sample will allow us to uncover properties of individual LAEs such as their stellar mass, star formation rate, dust attenuation, timing of stellar mass assembly, and the processes of star formation and quenching. Once completed, this work will help us to better understand the relationship between LAEs, their present-day analogs, and their primordial building blocks.

## Acknowledgments

This work utilizes observations at Cerro Tololo Inter-American Observatory, NSF’s NOIRLab (Prop. ID 2020B-0201; PI: K.-S. Lee), which is managed by the Association of Universities for Research in Astronomy under a cooperative agreement with the National Science Foundation.

This material is based upon work supported by the National Science Foundation Graduate Research Fellowship Program under grant No. DGE-2233066 to N.F. N.F. and E.G. would also like to acknowledge support from NASA Astrophysics Data Analysis Program grant 80NSSC22K0487 and NSF grant AST-2206222. N.F. would like to thank the LSSTDA Data Science Fellowship Program, which is funded by LSST Discovery Alliance, NSF Cybertraining grant No. 1829740, the Brinson Foundation, and the Moore Foundation; this participation in the program has benefited this work greatly. K.S.L. and V.R. acknowledge financial support from the National Science Foundation under grant No. AST-2206705 and from the Ross-Lynn Purdue Research Foundation grant. B. M. and Y.Y. are supported by the Basic Science Research Program through the National Research Foundation of Korea funded by the Ministry of Science, ICT & Future Planning (2019R1A2C4069803). L.G. and A.S. thank support from FONDECYT regular projects No. 1230591. H.S. acknowledges the support of the National Research Foundation of Korea grant No. 2022R1A4A3031306, funded by the Korean government (MSIT). The Institute for Gravitation and the Cosmos is supported by the Eberly College of Science and the Office of the Senior Vice President for Research at the Pennsylvania State University.

We thank Masami Ouchi for helpful comments on this paper. We also thank the anonymous referee for their thoughtful suggestions to improve this work.

## ORCID iDs

Nicole M. Firestone [ID](https://orcid.org/0000-0002-9811-2443) <https://orcid.org/0000-0002-9811-2443>  
 Eric Gawiser [ID](https://orcid.org/0000-0003-1530-8713) <https://orcid.org/0000-0003-1530-8713>  
 Vandana Ramakrishnan [ID](https://orcid.org/0000-0002-9176-7252) <https://orcid.org/0000-0002-9176-7252>  
 Kyoung-Soo Lee [ID](https://orcid.org/0000-0003-3004-9596) <https://orcid.org/0000-0003-3004-9596>  
 Francisco Valdes [ID](https://orcid.org/0000-0001-5567-1301) <https://orcid.org/0000-0001-5567-1301>  
 Changbom Park [ID](https://orcid.org/0000-0001-9521-6397) <https://orcid.org/0000-0001-9521-6397>  
 Yujin Yang [ID](https://orcid.org/0000-0003-3078-2763) <https://orcid.org/0000-0003-3078-2763>  
 Robin Ciardullo [ID](https://orcid.org/0000-0002-1328-0211) <https://orcid.org/0000-0002-1328-0211>  
 María Celeste Artale [ID](https://orcid.org/0000-0003-0570-785X) <https://orcid.org/0000-0003-0570-785X>  
 Caryl Gronwall [ID](https://orcid.org/0000-0001-6842-2371) <https://orcid.org/0000-0001-6842-2371>  
 Lucia Guaita [ID](https://orcid.org/0000-0002-4902-0075) <https://orcid.org/0000-0002-4902-0075>  
 Stephen Gwyn [ID](https://orcid.org/0000-0001-8221-8406) <https://orcid.org/0000-0001-8221-8406>  
 Ho Seong Hwang [ID](https://orcid.org/0000-0003-3428-7612) <https://orcid.org/0000-0003-3428-7612>  
 Sang Hyeok Im [ID](https://orcid.org/0009-0003-9748-4194) <https://orcid.org/0009-0003-9748-4194>  
 Woong-Seob Jeong [ID](https://orcid.org/0000-0002-2770-808X) <https://orcid.org/0000-0002-2770-808X>  
 Shreya Karthikeyan [ID](https://orcid.org/0009-0002-6186-0293) <https://orcid.org/0009-0002-6186-0293>  
 Dustin Lang [ID](https://orcid.org/0000-0002-1172-0754) <https://orcid.org/0000-0002-1172-0754>  
 Byeongha Moon [ID](https://orcid.org/0009-0008-4022-3870) <https://orcid.org/0009-0008-4022-3870>  
 Nelson Padilla [ID](https://orcid.org/0000-0001-9850-9419) <https://orcid.org/0000-0001-9850-9419>  
 Marcin Sawicki [ID](https://orcid.org/0000-0002-7712-7857) <https://orcid.org/0000-0002-7712-7857>  
 Eunsuk Seo [ID](https://orcid.org/0009-0007-1810-5117) <https://orcid.org/0009-0007-1810-5117>  
 Hyunmi Song [ID](https://orcid.org/0000-0002-4362-4070) <https://orcid.org/0000-0002-4362-4070>  
 Paulina Troncoso Iribarren [ID](https://orcid.org/0000-0001-6162-3023) <https://orcid.org/0000-0001-6162-3023>

## References

Acquaviva, V., Gawiser, E., & Guaita, L. 2011, *ApJ*, **737**, 47  
 Aihara, H., AlSayyad, Y., Ando, M., et al. 2019, *PASJ*, **71**, 114  
 Bertin, E., & Arnouts, S. 1996, *A&AS*, **117**, 393  
 Bradshaw, E., Almaini, O., Hartley, W., et al. 2013, *MNRAS*, **433**, 194  
 Brammer, G. B., Van Dokkum, P. G., Franx, M., et al. 2012, *ApJS*, **200**, 13  
 Broussard, A., Gawiser, E., Iyer, K., et al. 2019, *ApJ*, **873**, 74  
 Calzetti, D., Armus, L., Bohlin, R. C., et al. 2000, *ApJ*, **533**, 682  
 Cardamone, C., Schawinski, K., Sarzi, M., et al. 2009, *MNRAS*, **399**, 1191  
 Cassata, P., Le Fèvre, O., Garilli, B., et al. 2011, *A&A*, **525**, A143  
 Choi, J., Dotter, A., Conroy, C., et al. 2016, *ApJ*, **823**, 102  
 Ciardullo, R., Gronwall, C., Adams, J. J., et al. 2013, *ApJ*, **769**, 83  
 Ciardullo, R., Gronwall, C., Wolf, C., et al. 2011, *ApJ*, **744**, 110  
 Coil, A. L. 2013, Planets, Stars and Stellar Systems (Berlin: Springer), 387  
 Coil, A. L., Blanton, M. R., Burles, S. M., et al. 2011, *ApJ*, **741**, 8  
 Conroy, C., & Gunn, J. E. 2010, *ApJ*, **712**, 833  
 Conroy, C., Gunn, J. E., & White, M. 2009, *ApJ*, **699**, 486  
 Cool, R. J., Moustakas, J., Blanton, M. R., et al. 2013, *ApJ*, **767**, 118  
 Coupon, J., Czakon, N., Bosch, J., et al. 2018, *PASJ*, **70**, S7  
 Dey, A., Lee, K.-S., Reddy, N., et al. 2016, *ApJ*, **823**, 11  
 Dotter, A. 2016, *ApJS*, **222**, 8  
 Draine, B., & Li, A. 2007, *ApJ*, **657**, 810  
 Drinkwater, M. J., Byrne, Z. J., Blake, C., et al. 2018, *MNRAS*, **474**, 4151  
 Falcón-Barroso, J., Sánchez-Blázquez, P., Vazdekis, A., et al. 2011, *A&A*, **532**, A95  
 Fitzpatrick, E. L. 1999, *PASP*, **111**, 63  
 Garilli, B., Le Fèvre, O., Guzzo, L., et al. 2008, *A&A*, **486**, 683  
 Gawiser, E., Francke, H., Lai, K., et al. 2007, *ApJ*, **671**, 278  
 Gawiser, E., Van Dokkum, P. G., Gronwall, C., et al. 2006a, *ApJ*, **642**, L13  
 Gawiser, E., Van Dokkum, P. G., Herrera, D., et al. 2006b, *ApJS*, **162**, 1  
 Gebhardt, K., Cooper, E. M., Ciardullo, R., et al. 2021, *ApJ*, **923**, 217  
 Gronwall, C., Ciardullo, R., Hickey, T., et al. 2007, *ApJ*, **667**, 79  
 Guaita, L., Gawiser, E., Padilla, N., et al. 2010, *ApJ*, **714**, 255  
 Harish, S., Wold, I. G., Malhotra, S., et al. 2022, *ApJ*, **934**, 167  
 Hashimoto, T., Garel, T., Guiderdoni, B., et al. 2017, *A&A*, **608**, A10  
 Hu, E. M., Cowie, L. L., & McMahon, R. G. 1998, *ApJ*, **502**, L99  
 Huang, Y., Lee, K.-S., Cucciati, O., et al. 2022, *ApJ*, **941**, 134  
 Hui, L., & Gnedin, N. Y. 1997, *MNRAS*, **292**, 27  
 Iyer, K., & Gawiser, E. 2017, *ApJ*, **838**, 127  
 Iyer, K. G., Gawiser, E., Faber, S. M., et al. 2019, *ApJ*, **879**, 116  
 Kashikawa, N., Nagao, T., Toshikawa, J., et al. 2012, *ApJ*, **761**, 85  
 Kashino, D., Silverman, J. D., Sanders, D., et al. 2019, *ApJS*, **241**, 10  
 Kawanomoto, S., Uraguchi, F., Komiyama, Y., et al. 2018, *PASJ*, **70**, 66  
 Kerutt, J., Wisotzki, L., Verhamme, A., et al. 2022, *A&A*, **659**, A183  
 Kikuta, S., Ouchi, M., Shibuya, T., et al. 2023, *ApJS*, **268**, 24  
 Kollmeier, J. A., Zasowski, G., Rix, H.-W., et al. 2017, arXiv:1711.03234  
 Kunth, D., Mas-Hesse, J., Terlevich, E., et al. 1998, *A&A*, **334**, 11  
 Le Fèvre, O., Cassata, P., Cucciati, O., et al. 2013, *A&A*, **559**, A14  
 Le Fèvre, O., Saisse, M., Mancini, D., et al. 2003, *Proc. SPIE*, **4841**, 1670  
 Le Fèvre, O., Vettolani, G., Garilli, B., et al. 2005, *A&A*, **439**, 845  
 Lee, K.-S., Gawiser, E., Park, C., et al. 2024, *ApJ*, **962**, 36  
 Lilly, S. J., Le Brun, V., Maier, C., et al. 2009, *ApJS*, **184**, 218  
 Lilly, S. J., Le Fèvre, O., Renzini, A., et al. 2007, *ApJS*, **172**, 70  
 Madau, P. 1995, *ApJ*, **441**, 18  
 Maltby, D. T., Almaini, O., Wild, V., et al. 2016, *MNRAS: Letters*, **459**, L114  
 McLure, R., Pearce, H., Dunlop, J., et al. 2013, *MNRAS*, **428**, 1088  
 Nilsson, K. K., Tapken, C., Møller, P., et al. 2009, *A&A*, **498**, 13  
 Ouchi, M., Harikane, Y., Shibuya, T., et al. 2018, *PASJ*, **70**, S13  
 Ouchi, M., Ono, Y., & Shibuya, T. 2020, *ARA&A*, **58**, 617  
 Ouchi, M., Shimasaku, K., Akiyama, M., et al. 2008, *ApJS*, **176**, 301  
 Ouchi, M., Shimasaku, K., Furusawa, H., et al. 2003, *ApJ*, **582**, 60  
 Ouchi, M., Shimasaku, K., Furusawa, H., et al. 2010, *ApJ*, **723**, 869  
 Oyarzún, G. A., Blanc, G. A., González, V., Mateo, M., & Bailey, J. I. 2017, *ApJ*, **843**, 133  
 Padmanabhan, H., & Loeb, A. 2021, *A&A*, **646**, L10  
 Partridge, R. B., & Peebles, P. J. E. 1967, *ApJ*, **147**, 868  
 Paxton, B., Bildsten, L., Dotter, A., et al. 2011, *ApJS*, **192**, 3  
 Paxton, B., Cantiello, M., Arras, P., et al. 2013, *ApJS*, **208**, 4  
 Paxton, B., Marchant, P., Schwab, J., et al. 2015, *ApJS*, **220**, 15  
 Press, W., Rybicki, G., & Schneider, D. 1993, *ApJ*, **414**, 64  
 Pucha, R., Reddy, N. A., Dey, A., et al. 2022, *ApJ*, **164**, 159  
 Ramakrishnan, V., Moon, B., & Hyeok Im, S. 2023, *ApJ*, **951**, 119  
 Rhoads, J. E., Malhotra, S., Dey, A., et al. 2000, *ApJ*, **545**, L85  
 Salpeter, E. E. 1955, *ApJ*, **121**, 161  
 Sawicki, M., Arnouts, S., Huang, J., et al. 2019, *MNRAS*, **489**, 5202  
 Schenker, M. A., Ellis, R. S., Konidaris, N. P., & Stark, D. P. 2014, *ApJ*, **795**, 20  
 Schlafly, E. F., & Finkbeiner, D. P. 2011, *ApJ*, **737**, 103  
 Schlegel, D. J., Finkbeiner, D. P., & Davis, M. 1998, *ApJ*, **500**, 525  
 Scoggio, M., Guzzo, L., Garilli, B., et al. 2018, *A&A*, **609**, A84  
 Shapley, A. E., Steidel, C. C., Pettini, M., & Adelberger, K. L. 2003, *ApJ*, **588**, 65  
 Shi, K., Huang, Y., Lee, K.-S., et al. 2019, *ApJ*, **879**, 9  
 Silverman, J. D., Kashino, D., Sanders, D., et al. 2015, *ApJS*, **220**, 12  
 Skelton, R. E., Whitaker, K. E., Momcheva, I. G., et al. 2014, *ApJS*, **214**, 24  
 Stark, D. P., Ellis, R. S., Chiu, K., Ouchi, M., & Bunker, A. 2010, *MNRAS*, **408**, 1628  
 Steidel, C. C., Adelberger, K. L., Giavalisco, M., Dickinson, M., & Pettini, M. 1999, *ApJ*, **519**, 1  
 Vargas, C. J., Bish, H., Acquaviva, V., et al. 2014, *ApJ*, **783**, 26  
 Venemans, B., Röttgering, H., Miley, G., et al. 2005, *A&A*, **431**, 793  
 Walker-Soler, J. P., Gawiser, E., Bond, N. A., Padilla, N., & Francke, H. 2012, *ApJ*, **752**, 160  
 Weaver, J. R., Kauffmann, O., Ilbert, O., et al. 2022, *ApJS*, **258**, 11  
 Weiss, L. H., Bowman, W. P., Ciardullo, R., et al. 2021, *ApJ*, **912**, 100  
 Yoshioka, T., Kashikawa, N., Inoue, A. K., et al. 2022, *ApJ*, **927**, 32  
 Zheng, Z.-Y., Wang, J., Rhoads, J., et al. 2017, *ApJ*, **842**, L22